

# Direct Recycling of All-Solid-State Batteries with a Halide Solid Electrolyte via Water-Based Separation: Interactions of Electrode Materials in Aqueous $\text{Li}_3\text{InCl}_6$ Solutions

Martine Jacob, Harol Moreno Fernández, Aaron Haben, Aamir Iqbal Waidha, Simay Öznel, Jan P. Hofmann, Ralf Kautenburger, Oliver Clemens,\* and Kerstin Wissel\*

Despite extensive research in the field of all-solid-state batteries, there has been limited attention to their recycling, which is crucial for achieving long-term sustainability. Different electrolyte and electrode combinations must be considered for the recycling of these batteries, each requiring a detailed investigation of potential recycling approaches. The halide-based solid electrolyte,  $\text{Li}_3\text{InCl}_6$ , has attracted significant attention due to its high-room-temperature lithium-ion conductivity and its ability to recover its initial crystal structure after dissolution in water without significant electrochemical deterioration. This structural reversibility could potentially enable a direct recycling approach, allowing for the separation

of the electrolyte from active electrode materials when dissolved in  $\text{H}_2\text{O}$ . To assess the recycling compatibility, the interactions of  $\text{Li}_3\text{InCl}_6$  with different electrode materials ( $\text{Li}_4\text{Ti}_5\text{O}_{12}$ ,  $\text{LiCoO}_2$ ,  $\text{LiMn}_2\text{O}_4$ , carbon-coated  $\text{LiFePO}_4$ ,  $\text{LiNi}_{0.8}\text{Mn}_{0.1}\text{Co}_{0.1}\text{O}_2$ , and  $\text{LiNi}_{0.8}\text{Co}_{0.15}\text{Al}_{0.05}\text{O}_2$ ) are studied during dissolution. Interactions arising from Lewis-acid and Lewis-base reactions can be identified using a combination of X-ray diffraction, X-ray photoelectron spectroscopy, and inductively coupled plasma mass spectrometry. Depending on the material combination, these interactions significantly impact the electrochemical properties of both recycled  $\text{Li}_3\text{InCl}_6$  and the electrode materials compared to the pristine samples.

## 1. Introduction

Driven by the impact of climate change and the pursuit of reducing  $\text{CO}_2$  emissions, the demand for sustainable energy technologies is increasing globally. Lithium-ion batteries (LIBs) are widely used in portable electronic devices and electromobility-related applications.<sup>[1]</sup> However, these batteries suffer from safety issues due to the use of flammable organic liquid electrolytes. These

safety issues can be mitigated by substituting the organic liquid electrolyte with a solid-state electrolyte (SSE), resulting in so-called all-solid-state batteries (ASSBs). Such batteries offer the potential for higher gravimetric and volumetric energy densities and enhanced safety compared to conventional LIBs, which has generated significant research interest from both academia and industry.<sup>[2–4]</sup>

The research field for ASSBs is diverse, including the investigation and development of different solid electrolyte classes (e.g., oxides, sulfides, halides, and polymers), optimizing electrode designs, understanding and controlling the interfaces between solid electrolyte and electrode materials, and scaling up for potential applications. Despite the extensive efforts to realize their future application and extend their lifetime, ASSBs will inevitably reach their end-of-life (EoL). These batteries may contain critical raw materials (CRMs) to varying degrees, depending on the material combinations used, including lithium (Li), cobalt (Co), indium (In), etc., which are all vital for the advancement of sustainable energy technologies. Reintegrating these CRMs into the material cycle is essential to ensure the continuity of the battery supply chain. The criticality, environmental impacts (e.g., pollution, resource depletion), and geopolitical significance of these CRMs present a substantial risk for supply chain disruption if they are not recovered from EoL batteries.<sup>[5]</sup>

Existing recycling approaches for conventional LIBs (i.e., pyrometallurgy, hydrometallurgy, and direct recycling) face limitations when applied to industrial-scale operations.<sup>[1,5]</sup> These challenges arise in part because conventional LIBs were not originally designed with recyclability in mind,<sup>[6]</sup> and the current lack of economic feasibility<sup>[7]</sup> further complicates the issue. The recycling of ASSBs presents even greater challenges due to a multitude of different

M. Jacob, A. I. Waidha, S. Öznel, O. Clemens, K. Wissel  
Institute for Materials Science  
Materials Synthesis Group  
University of Stuttgart  
Heisenbergstraße 3, 70569 Stuttgart, Baden-Wuerttemberg, Germany  
E-mail: oliver.clemens@imw.uni-stuttgart.de  
kerstin.wissel@imw.uni-stuttgart.de

H. Moreno Fernández, J. P. Hofmann  
Department of Materials and Geosciences  
Surface Science Laboratory  
Technical University of Darmstadt  
Peter-Grünberg-Straße 4, 64287 Darmstadt, Germany

A. Haben, R. Kautenburger  
Inorganic Solid State Chemistry  
Saarland University  
Elemental Analysis Campus C4 1, 66123 Saarbrücken, Germany

A. I. Waidha  
Research and Development  
theion GmbH  
Gerhard-Sedlmayr-Straße 31, 12487 Berlin, Germany

 Supporting information for this article is available on the WWW under https://doi.org/10.1002/batt.202500189

 © 2025 The Author(s). *Batteries & Supercaps* published by Wiley-VCH GmbH. This is an open access article under the terms of the Creative Commons Attribution License, which permits use, distribution and reproduction in any medium, provided the original work is properly cited.

SSE chemistries. These design differences make conventional LIB recycling methods unsuitable for direct adaptation, requiring the development of new strategies to address the unique challenges posed by ASSBs. Since ASSBs are still under development and have not yet achieved large-scale commercial implementation and availability, there is a valuable opportunity to integrate recycling considerations into the development and design process.<sup>[1,5]</sup> This integration is crucial for addressing materials criticality, ensuring responsible resource utilization, minimizing environmental impact, and assessing the recycling compatibility of materials (e.g., SSEs in combination with electrode materials). Therefore, developing comprehensive recycling strategies specifically tailored to ASSBs is an essential area of research. Such efforts will contribute to the responsible use of materials, efficient EoL management, and overall sustainability of these batteries, aligning with broader goals related to sustainability and a circular economy.

To develop a circular concept for ASSBs that emphasizes full recyclability and reusability, the halide-based solid electrolyte  $\text{Li}_3\text{InCl}_6$  presents a promising option. Recent research by Li et al.<sup>[8]</sup> highlights a water-mediated, one-pot synthesis method for  $\text{Li}_3\text{InCl}_6$ . This method involves dissolving anhydrous  $\text{LiCl}$  and  $\text{InCl}_3$  in deionized  $\text{H}_2\text{O}$ , followed by evaporation and subsequent thermal treatment at 200 °C under vacuum. Remarkably, this process allows crystalline and stoichiometric  $\text{Li}_3\text{InCl}_6$  to be regenerated after redissolution in  $\text{H}_2\text{O}$  and subsequent water evaporation. After an additional crystallization step, the material's initial ionic conductivity ( $\approx 2.05 \times 10^{-3} \text{ S cm}^{-1}$ ) is recovered.<sup>[8]</sup> This structural reversibility, without significant electrochemical performance deterioration, motivates the exploration of its recycling potential. Incorporating electrode materials into the recrystallization process increases its complexity, necessitating the development of efficient separation strategies. Furthermore, minimizing material loss (i.e., an increasing recovery rate) would enhance the entire process's sustainability and economic viability.

Pyrometallurgy, hydrometallurgy, and direct recycling are three conventional recycling methods.<sup>[2,5,9,10]</sup> Among them, pyrometallurgy is likely to be of lower relevance for the recycling of  $\text{Li}_3\text{InCl}_6$  due to potential cross-reactions with the electrode material in the molten state, leading to the formation of oxychlorides.<sup>[5]</sup> Hydrometallurgy involving acids and bases may not be applicable in this context, as the use of strong acids (e.g., hydrochloric acid ( $\text{HCl}$ ), sulfuric acid ( $\text{H}_2\text{SO}_4$ ), and nitric acid ( $\text{HNO}_3$ )) is not required to dissolve the SSE, thereby preventing undesired leaching of electrode materials. Consequently, a direct recycling method, specifically a dissolution-based separation method, could be viable if the SSE can be dissolved in  $\text{H}_2\text{O}$  and recrystallized while leaving the undissolved electrode materials unaffected.

To support the integration of recycling strategies into the battery design process, the compatibility and recyclability of  $\text{Li}_3\text{InCl}_6$  with different commercially relevant oxide-based electrode materials (e.g.,  $\text{Li}_4\text{Ti}_5\text{O}_{12}$  (LTO),  $\text{LiCoO}_2$  (LCO),  $\text{LiMn}_2\text{O}_4$  (LMO), C-coated  $\text{LiFePO}_4$  (C-LFP),  $\text{LiNi}_{0.8}\text{Mn}_{0.1}\text{Co}_{0.1}\text{O}_2$  (NMC811), and  $\text{LiNi}_{0.8}\text{Co}_{0.15}\text{Al}_{0.05}\text{O}_2$  (NCA)) during dissolution in  $\text{H}_2\text{O}$  are investigated in this article. Additionally, elemental, structural, and electrochemical characterization of all materials before and after separation are performed. Thus, reactive interactions between  $\text{Li}_3\text{InCl}_6$  and individual electrode materials are identified

for these idealized mixtures, (i.e., excluding components such as the Li metal anode, current collectors, additives such as binding material, and graphite). By this, we aim to provide insights into the suitability of chloride electrolytes for direct recycling approaches, while also highlighting potential limitations arising from side reactions with oxides in aqueous solutions during the recycling process.

## 2. Results and Discussion

### 2.1. Structural Characterization of Pristine Electrolyte and Electrode Materials

The solid electrolyte  $\text{Li}_3\text{InCl}_6$  and the oxide-based electrode materials (e.g., LTO, LCO, LMO, C-LFP, NMC, and NCA) were synthesized as described in experimental section and characterized using XRD and Rietveld analysis (see Figure S1a and S4, Supporting Information).

$\text{Li}_3\text{InCl}_6$  crystallizes in the monoclinic space group  $C2/m$ , with lattice parameters  $a = 6.41008(17) \text{ \AA}$ ,  $b = 11.0782(3) \text{ \AA}$ ,  $c = 6.3833(2) \text{ \AA}$ , and  $\beta = 109.7807(2)^\circ$ , consistent with previously reports.<sup>[8]</sup> Layer-like structures with a honeycomb arrangement, such as  $\text{Li}_3\text{InCl}_6$ , are known to exhibit stacking faults. Rietveld analysis (see Figure S1a, Supporting Information) reveals a misfit due to significant anisotropic broadening of specific reflections, including  $(020)$ ,  $(110)$ ,  $(11\bar{1})$ ,  $(021)$ , and  $(111)$ , indicating the presence of stacking faults.<sup>[11,12]</sup> Additionally, a broad triangular-shaped increase in "background" intensity underneath this group of reflections at low diffraction angles is typically associated with stacking faults.<sup>[13,14]</sup> While this feature has been reported in previous studies, it is not observed in the present measurements, likely due to the use of a different radiation wavelength or its correlation with reflections of the airtight sample holder. Consequently, the structural analysis was carried out using the model reported by Li et al.<sup>[8]</sup> in which stacking faults were not considered. Although not discussed further in this study, it should be noted that all  $\text{Li}_3\text{InCl}_6$  samples exhibit stacking faults to some degree. A detailed analysis of these defects, however, falls beyond the scope of this work.

All electrode materials were synthesized with high purity, as confirmed by Rietveld refinement (Figure S4, Supporting Information). The calculated lattice parameters are summarized in Table S3, Supporting Information.

### 2.2. Recrystallization Behavior of $\text{Li}_3\text{InCl}_6$

To confirm the reversibility of the formation of  $\text{Li}_3\text{InCl}_6$  after redissolution, the pristine  $\text{Li}_3\text{InCl}_6$  was dissolved in distilled  $\text{H}_2\text{O}$  and subsequently recrystallized. The recorded diffraction pattern (see Figure S1b, Supporting Information) demonstrates that  $\text{Li}_3\text{InCl}_6$  can be successfully recrystallized after redissolution in  $\text{H}_2\text{O}$ . Small changes in the lattice parameters were observed (see Table S1, Supporting Information), which may originate from subtle structural changes such as a low degree of Li-In disorder. These structural changes cannot be accurately identified by

diffraction analysis alone and necessitate complementary methods (see section 2.3.1).

### 2.3. Dissolution-Based Separation Process

After confirming the recovery of crystalline  $\text{Li}_3\text{InCl}_6$  after redissolution, the process was extended to more complex conditions by incorporating electrode materials (e.g., LTO, LCO, LMO, C-LFP, NMC, and NCA). As described in the experimental section,  $\text{Li}_3\text{InCl}_6$  was selectively dissolved in distilled  $\text{H}_2\text{O}$ , allowing for the separation of the undissolved electrode materials. The following section examines the extent of interaction between the electrolyte and different electrode materials during the recycling process, providing insights into potential materials compatibility and recovery efficiency.

#### 2.3.1. Investigation of Recycled Electrolyte Materials

Figure 1a shows the diffraction patterns of the recycled  $\text{Li}_3\text{InCl}_6$  after separation from different electrode materials and subsequent

recrystallization. All diffraction patterns (see Figure S2, Supporting Information) and the determined lattice parameters (see Table S1, Supporting Information) confirm the successful recovery of crystalline  $\text{Li}_3\text{InCl}_6$ . Rietveld analysis reveals deviations in the lattice parameters compared to those of the pristine sample. The relative change in cell volume, in relation to the volume of the pristine sample, is given in Figure S3, Supporting Information. It was observed that the cell volumes increased for all recycled electrolytes, except for the recycled  $\text{Li}_3\text{InCl}_6$ , after separation from NCA. These variations in lattice parameters may be attributed to ion-exchange processes, which result in alternations in the Li-In-Cl ratio.

It is important to note that, in addition to the main phase, and unlike dissolution–recrystallization of the pure electrolyte, LiCl is observed as an additional impurity phase. Remarkably, the extent of this impurity phase varies depending on the electrode material from which the electrolyte was separated from (see Table S1, Supporting Information). For instance, only a small amount of LiCl is detected after separation from LTO, LCO, and LMO. A higher fraction of LiCl is observed with Ni-rich electrode materials (e.g., NMC and NCA). Notably, no additional LiCl formation was detected with C-coated LFP. The presence of LiCl impurity within

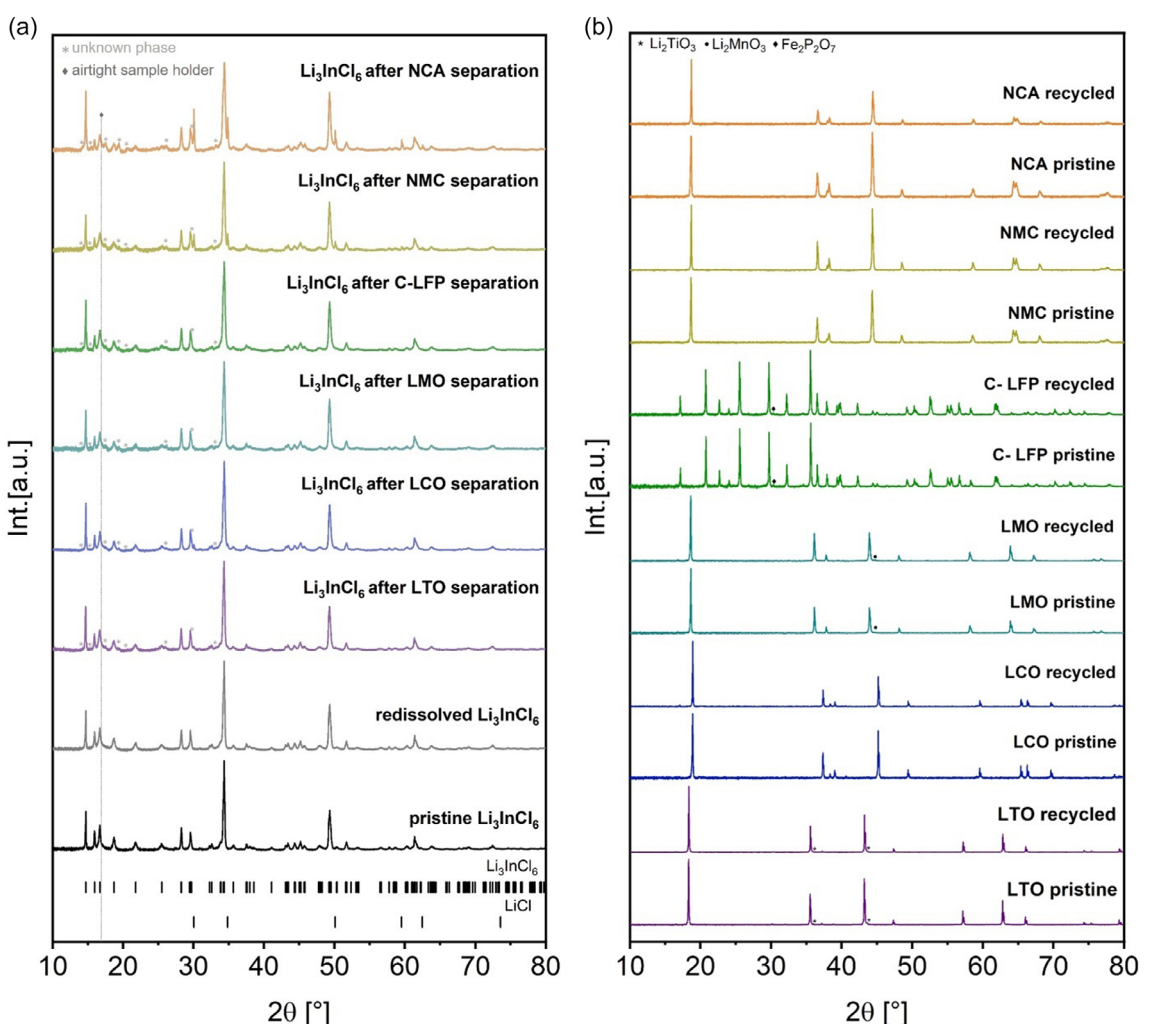


**Figure 1.** XRD patterns of a) pristine, redissolved, and recycled  $\text{Li}_3\text{InCl}_6$  after separation from different electrode materials and b) pristine and recycled electrode materials.

the recycled  $\text{Li}_3\text{InCl}_6$  suggests a potential loss and/or transfer of indium from the electrolyte, resulting in incomplete recrystallization of  $\text{Li}_3\text{InCl}_6$ . As discussed in section 2.3.2, the indium loss and/or transfer occurs at the surface of the electrode materials. Additionally, the varying amounts of  $\text{LiCl}$  impurity after the separation of different electrode materials are described in more detail in section 2.4.

In addition to the  $\text{LiCl}$  impurity phase, an unknown phase was observed in recycled  $\text{Li}_3\text{InCl}_6$ , characterized by reflections at  $2\theta = 14.27^\circ, 15.47^\circ, 17.53^\circ, 19.37^\circ, 20.76^\circ$ , and  $26.14^\circ$ . This phase was particularly prominent in the recycled  $\text{Li}_3\text{InCl}_6$  after separation from NCA. Although its exact composition remains unknown, this impurity phase has been observed across multiple measurements.

A possible explanation for the additional phase is the formation of a metal oxy- or hydroxychloride under nonsaturated HCl conditions. During recycling, this phase may arise from the reaction between the halide and the oxide electrode, which exhibits basic properties<sup>[15–17]</sup> (see section 2.4).

Further evidence supporting this hypothesis comes from  $\text{Li}_3\text{InCl}_6$  synthesis under insufficient vacuum conditions, where both  $\text{Li}_3\text{InCl}_6$  and the impurity phase were observed (see Figure S5, Supporting Information). Higher pressure during heating (e.g., 0.060 vs. 0.017 mbar) could promote interaction with ambient moisture, leading to partial hydrolysis and the formation of a metal oxy- or hydroxychloride.

Alternatively, this phase may result from variations in the Li-In-Cl ratio. A systematic study on stoichiometric variations based on  $\text{Li}_{3-6x}\text{In}_{1+2x}\text{Cl}_6$  ( $-0.5 \leq x \leq 0.5$ ) showed that at  $x = -0.1$  ( $\text{Li}_{3.6}\text{In}_{0.8}\text{Cl}_6$ ),  $\text{Li}_3\text{InCl}_6$ ,  $\text{LiCl}$ , and the impurity phase were present (see Figure S7, Supporting Information).

Despite the inability to definitively identify this impurity phase, an effort was made to quantify its relative phase fraction in the recycled electrolytes by analyzing the integrated intensity of the unidentified reflections (see Table S2, Supporting Information) and relating it to the overall integrated intensity of the identified crystalline phases. The results indicate that this unknown phase has a significantly higher fraction in recycled  $\text{Li}_3\text{InCl}_6$  after separation from NCA compared to other recycled materials. This suggests that the interaction between the electrolyte and Ni-rich electrode materials is more pronounced during recycling.

Further, the stoichiometric variation study of  $\text{Li}_3\text{InCl}_6$  shows that when the composition becomes Li rich, the system forms a mixture of  $\text{Li}_3\text{InCl}_6$  and  $\text{LiCl}$ , rather than a substochiometric  $\text{Li}_3\text{InCl}_6$ . This aligns with the observations during recycling, where indium from  $\text{Li}_3\text{InCl}_6$  is transferred to the electrode materials (as confirmed by XPS findings reported in section 2.3.2 and ICP-MS analysis in the next paragraph), leading to indium depletion in the electrolyte. Consequently,  $\text{LiCl}$  forms as a secondary phase, reflecting the Li-rich, In-deficient composition. These findings suggest that  $\text{Li}_3\text{InCl}_6$  remains stable at its expected stoichiometry, with  $\text{LiCl}$  forming when indium is lost during recycling.

To further verify the depletion of indium in the electrolyte after the recycling process, ICP-MS analysis was conducted on all  $\text{Li}_3\text{InCl}_6$  electrolyte samples. These measurements assessed their detailed chemical compositions and identified potential cross-contamination from recycling with different electrode materials

(see Table S5–S7, Supporting Information). All measurements were normalized to lithium (or chlorine), revealing deviations in the molar ratios of ions after recycling (see Table S6, Supporting Information). A noticeable increase in lithium content in the recrystallized fraction was observed, likely due to ion exchange processes, such as  $\text{Li}^+$ / $\text{H}^+$  exchange between the electrode material and  $\text{H}_2\text{O}$ .  $\text{Li}^+$  ions from the electrode materials dissolve in  $\text{H}_2\text{O}$ <sup>[15,18,19]</sup> and likely coprecipitate along with  $\text{Li}_3\text{InCl}_6$  during recrystallization.

Consequently, the recycled  $\text{Li}_3\text{InCl}_6$  exhibits a higher lithium content than the pristine material. This increase could result from small compositional changes in the recrystallized  $\text{Li}_3\text{InCl}_6$  (in line with slight lattice parameter variations) and/or residual  $\text{LiCl}$ . The indium-to-chloride ratio decreases after recycling. Notably,  $\text{Li}_3\text{InCl}_6$  separated from Ni-rich electrodes shows a lower indium content compared to other electrode materials, suggesting significant indium losses during the recycling process.

Moreover, transition metal (TM) dissolution occurs during recycling in  $\text{H}_2\text{O}$ , a phenomenon that had been previously reported for oxide-based electrode materials in other studies.<sup>[15,16,19]</sup> In this study, during the recycling process, Mn ions ( $\approx 0.09\%$ ) from LMO and Fe ions ( $\approx 0.02\%$ ) from C-LFP were detected in the recycled  $\text{Li}_3\text{InCl}_6$ . Increased amounts of TMs are found in  $\text{Li}_3\text{InCl}_6$  recycled from NMC and NCA, with 0.02% Ni ions detected after separation from NMC and, 0.12% Ni ions, 0.05% Co ions, and 0.22% Al ions detected after separation from NCA. The dissolution of Co ions from NCA is visually apparent, evidenced by a blue discoloration at the bottom of the flask upon evaporation (see Figure S6, Supporting Information). This discoloration can be attributed to the transferred cobalt species. Thus, the ICP-MS analysis of pristine, redissolved, and recycled  $\text{Li}_3\text{InCl}_6$  after separation from different electrode materials highlights significant compositional changes and different Li-In-Cl ratios, with the dissolution of Li and TM ions from different electrode materials partially acting as dopants in the recycled electrolyte.

As derived from the analysis of the diffraction patterns (see Figure 1a), structural and compositional changes can occur on recrystallization in the presence of different electrodes. SEM imaging was performed to assess the potential impact on the materials morphology. Figure 2 presents SEM images illustrating the morphology of pristine, redissolved, and recycled  $\text{Li}_3\text{InCl}_6$  after separation from different electrode materials. The particle size distribution of all samples was analyzed using statistical parameters, including the average particle size ( $d_{\text{ave}}$ ) and the modal particle size ( $d_m$ ), as shown in the histograms in Supporting Information (Figure S8, Supporting Information).

The pristine  $\text{Li}_3\text{InCl}_6$  (Figure 2a) exhibits agglomerated particles with irregular shapes and a multimodal particle size distribution. The redissolved  $\text{Li}_3\text{InCl}_6$  (Figure 2b), along with the recycled  $\text{Li}_3\text{InCl}_6$  after separation from LTO, LCO, LMO, and C-LFP (Figure 2c–f), displays morphologies that are largely consistent with the pristine material. Although all samples underwent identical  $\text{H}_2\text{O}$  evaporation and recrystallization conditions, distinct differences emerge in the recycled  $\text{Li}_3\text{InCl}_6$  after separation from NMC (Figure 2g) and NCA (Figure 2h). Both samples exhibit increased particle agglomeration, forming larger clusters with a more compact structure compared to the pristine material.

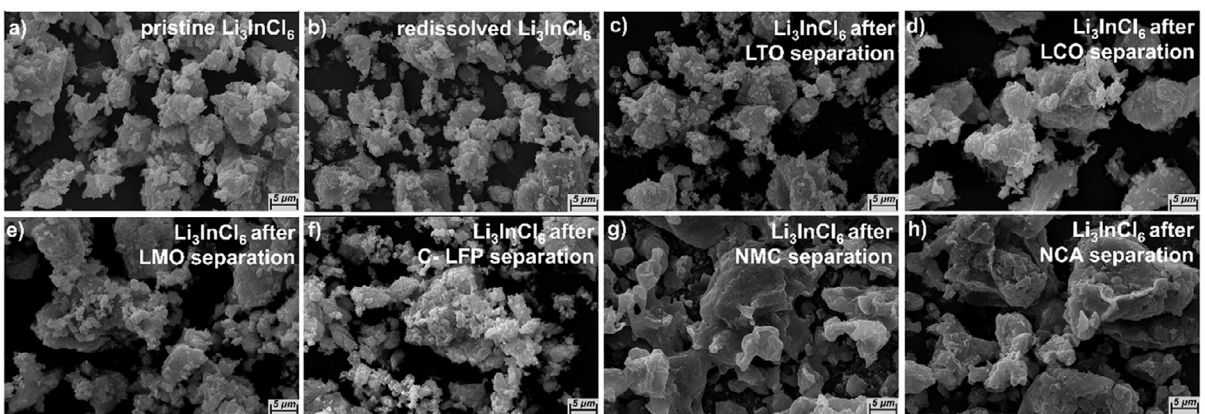


**Figure 2.** SEM images of a) pristine  $\text{Li}_3\text{InCl}_6$ , b) redissolved  $\text{Li}_3\text{InCl}_6$ , recycled  $\text{Li}_3\text{InCl}_6$  after separation from c) LTO, d) LCO, e) LMO, f) C-LFP, g) NMC, and h) NCA.

These morphological variations correlate with the particle size distribution data. While pristine, redissolved, and recycled  $\text{Li}_3\text{InCl}_6$  separated from LTO, LCO, LMO, and C-LFP exhibit relatively narrow particle size distributions, samples separated from NMC and NCA display broader distributions with increased  $d_{ave}$  and  $d_m$ , suggesting that interactions during the recycling process influence recrystallization behavior of  $\text{Li}_3\text{InCl}_6$ .

The increased agglomeration in these samples may be attributed to the dissolution of TMs (e.g., Ni, Mn, Co, Al) during the recycling process, as confirmed by ICP-MS measurements (Table S6, Supporting Information). These dissolved TMs likely impact the recrystallization behavior, altering nucleation and growth,<sup>[20]</sup> which leads to significant morphological changes compared to  $\text{Li}_3\text{InCl}_6$  separated from other electrode materials.

This increased degree of agglomeration could potentially impact the electrochemical properties of the recycled electrolyte (see section 2.5.1).

### 2.3.2. Investigation of Recycled Electrode Materials

The preceding results indicate that interactions between the solid electrolyte and electrode materials occur during the dissolution-based separation process. The diffraction patterns of the recovered electrodes are analyzed to assess whether these interactions have induced degradation in the electrode materials, as shown in Figure 1b and Figure S4, Supporting Information. The electrode materials exhibit minimal changes in their diffraction patterns compared to the pristine material, with only slight variations of lattice parameters observed, as detailed in Table S2, Supporting Information. As described earlier, the presence of LiCl in the recycled electrolyte indicates that indium ions might be transferred to the electrode materials during the dissolution process. The absence of crystalline In-rich impurity phases in the diffraction patterns of both the recovered electrolyte and the electrode materials indicates that the indium may be present in an amorphous phase within the materials, adsorbed on the surface of the individual electrode materials forming surface layers or through partial substitution of TM ions from the electrode materials with  $\text{In}^{3+}$  ions. The minimal changes observed in lattice parameters between the

pristine and recovered electrode materials further support that the crystalline phase remains largely unchanged, indicating that any topochemical ion exchange reactions are likely confined to the particles surfaces or regions near the surface<sup>[21]</sup> rather than occurring homogeneously throughout the bulk.

Given that XRD is not surface sensitive, XPS was employed to investigate the surface characteristics of both the pristine and recycled electrode materials. The primary focus of this analysis was the In 3d spectrum, aiming to assess the formation of indium-rich layers or precipitates on the electrode surface during recycling. Additionally, the chemical states of TMs were examined to identify surface-related changes indicative of potential degradation process.

**Figure 3** presents the In 3d XP spectra of recycled electrode materials, showing two distinct peaks corresponding to  $\text{In} 3d_{5/2}$  and  $\text{In} 3d_{3/2}$  peaks. These are attributed to In-O species (e.g., indium oxide ( $\text{In}_2\text{O}_3$ )), with an energy separation of  $\approx 7.5$  eV, consistent with values reported in literature.<sup>[22,23]</sup> The layered electrode materials (e.g., LCO, NMC, and NCA) exhibit additional indium-containing species, including In-OH (e.g.,  $\text{In(OH)}_3$ )<sup>[22,23]</sup> and In-Cl (e.g.,  $\text{InCl}_3$ ),<sup>[22,23]</sup> indicating the presence of these species at the surface, in contrast to spinel-type (e.g., LTO and LMO) and olivine-type materials (C-LFP). This observation aligns with the increased amounts of LiCl alongside the targeted  $\text{Li}_3\text{InCl}_6$  phase, as shown in Figure 1a and discussed in the previous section. The mechanism underlying the formation of the In-rich surface layer is further elaborated in section 2.4.

After confirming the indium transfer to the electrode materials, XPS analysis was extended to TM 2p spectra (**Figure 4**) to evaluate surface degradation induced by the recycling process. The main TM 2p spectra are presented in Figure 4, while additional spectra for other TMs, as well as Li 1s, and O 1s, can be found in the Supplementary Information (Figure S9–S11, Supporting Information).

For pristine LTO, the  $\text{Ti} 2p_{3/2}$  peak at 459.4 eV corresponds to the  $\text{Ti}^{4+}$  (see Figure 4a), with additional lower binding energy peaks at 457.7 and 455.6 eV assigned to  $\text{Ti}^{3+}$  and  $\text{Ti}^{2+}$ , respectively. These reductions likely result from Ar ion-induced damage during sputter cleaning before the analysis, as previously reported.<sup>[24]</sup> In the recycled LTO sample, the  $\text{Ti} 2p_{3/2}$  peak position

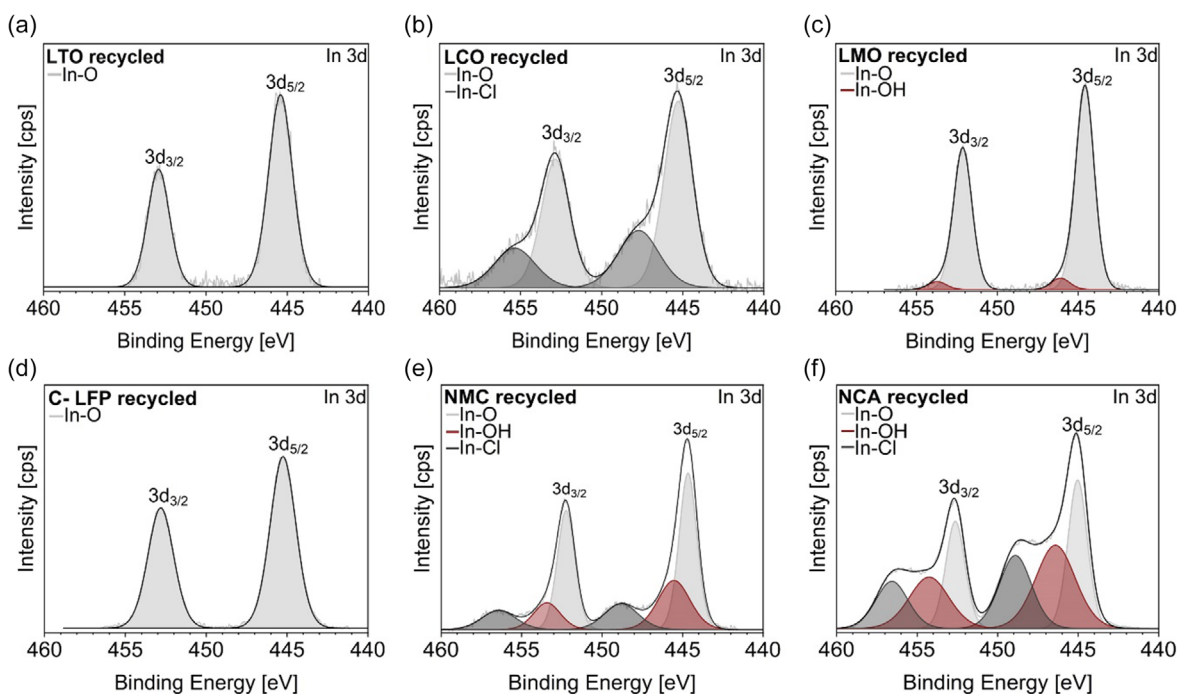


Figure 3. XPS measurements of recycled electrode materials. In 3d spectrum of recycled: a) LTO, b) LCO, c) LMO, d) C-LFP, e) NMC, and f) NCA.

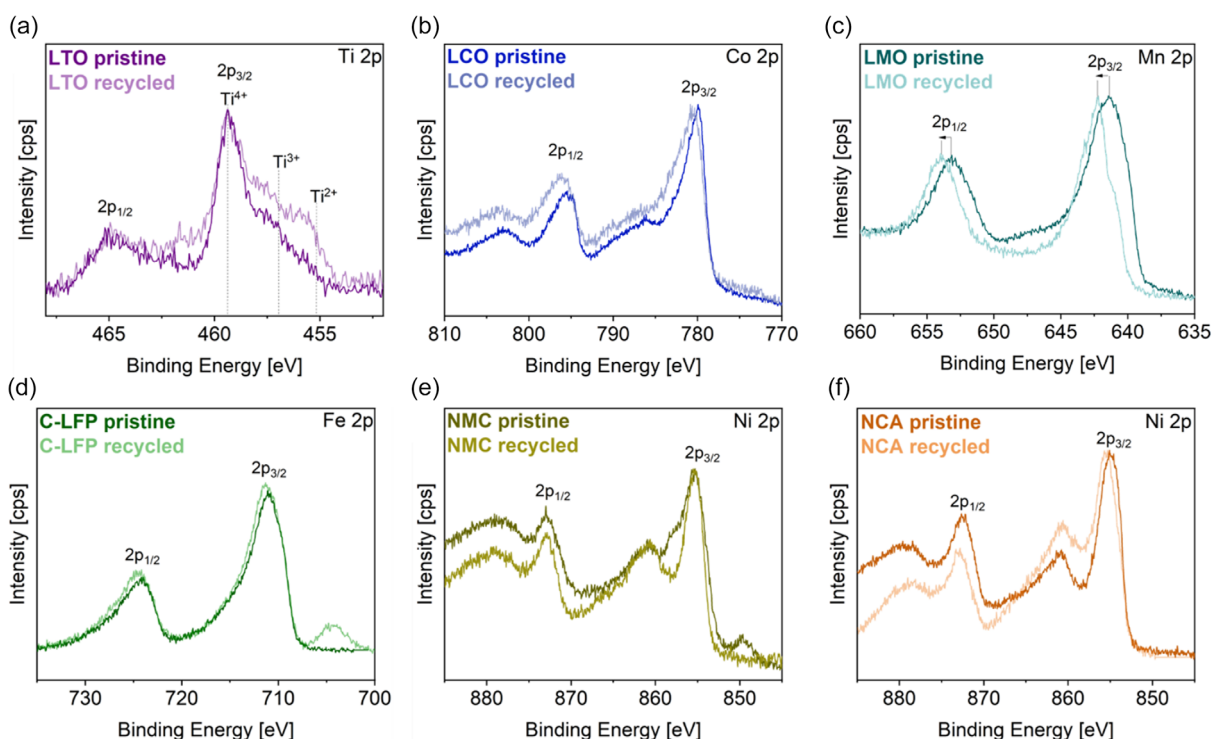


Figure 4. XPS comparison of TM core level of pristine and recycled: a) LTO, b) LCO, c) LMO, d) C-LFP, e) NMC, and f) NCA.

remains unchanged, indicating the preservation of  $\text{Ti}^{4+}$ . However, the increased intensity of the  $\text{Ti}^{3+}$  and  $\text{Ti}^{2+}$  peaks suggests a higher degree of titanium reduction. Despite this observation, the intrinsic stability of  $\text{Ti}^{4+}$  renders its reduction during recycling unlikely. Furthermore, no significant shifts are observed in the O

1s (Figure S9a,b, Supporting Information) and Li 1s spectra (Figure S10a, Supporting Information), indicating minimal changes in the lithium and oxygen chemical states.

For pristine LCO, the Co 2p<sub>3/2</sub> spectrum displays a peak at 780.0 eV, corresponding to a mixed  $\text{Co}^{3+}/\text{Co}^{2+}$  oxidation state

(Figure 4b), attributed to  $\text{Co}_3\text{O}_4$  precursor materials.<sup>[25]</sup> In the recycled sample, no peak shift is observed. However, peak broadening suggests the reduction of  $\text{Co}^{3+}$  to  $\text{Co}^{2+}$ , potentially due to  $\text{Co}(\text{OH})_2$ <sup>[26]</sup> formation on the surface. This is further supported by the broadening observed in the O 1s spectrum (Figure S9c,d, Supporting Information). Additionally, the Li 1s spectrum (Figure S10b, Supporting Information) shows a peak shift from 54.5 eV in the pristine sample, indicative of surface  $\text{LiOH}$ ,  $\text{Li}_2\text{O}$ , and  $\text{Li}_2\text{CO}_3$ , to 56.1 eV in the recycled sample, consistent with LiCl formation due to surface modification.

For pristine LMO, the Mn 2p<sub>3/2</sub> peaks range from ≈640.3 to 643.9 eV, indicating mixed  $\text{Mn}^{2+}$ ,  $\text{Mn}^{3+}$ , and  $\text{Mn}^{4+}$  oxidation states (see Figure 4c). After recycling, the peaks shift toward higher binding energies (642.3 eV), suggesting an increase in  $\text{Mn}^{4+}$  at the surface. This indicates that  $\text{Mn}^{3+}$  disproportionation occurred under aqueous conditions,<sup>[27]</sup> leading to Mn dissolution, as confirmed by ICP-MS. Some dissolved Mn ions may have reprecipitated as  $\text{Mn}(\text{OH})_2$ ,<sup>[28]</sup> as indicated by O 1s broadening (Figure S9e,f, Supporting Information), although oxidation remains the dominant surface transformation.<sup>[27]</sup> The Li 1s spectrum remains unchanged (Figure S10c, Supporting Information).

For pristine C-LFP, the Fe 2p<sub>3/2</sub> peaks appear at ≈710.9 and 724.7 eV, corresponding to  $\text{Fe}^{2+}/\text{Fe}^{3+}$  oxidation states (see Figure 4d). After recycling, peak broadening, suggests possible surface modifications, such as hydroxylation, which is further supported by changes in the O 1s spectrum (Figure S9g,h, Supporting Information). Additionally, a new peak emerges at 704.2 eV, corresponding to In 3p<sub>1/2</sub>. The P 2p spectrum, centered at 133.2 eV, remains consistent with P—O bonding in both pristine and recycled samples (Figure S11a, Supporting Information), while the Li 1s core-level spectrum shows no detectable changes after recycling (Figure S10d, Supporting Information).

For pristine NMC in Figure 1e, the Ni 2p<sub>3/2</sub> peaks exhibit binding energies ranging from ≈855.3 to 857.9 eV, corresponding to NiO, with the latter peak suggestive of a hydroxide species (e.g.,  $\text{Ni}(\text{OH})_2$  or  $\text{NiOOH}$ ).<sup>[29–31]</sup> Additionally, an unidentified fluorine-related peak at ≈849.7 eV is observed. This peak can be attributed to F 1s signal and its Auger peaks at 832.0 and 858.9 eV, the latter overlapping with Ni 2p<sub>3/2</sub> peak. After recycling, the spectrum shows a single peak at 855.4 eV, attributed to a hydroxide species. The Mn 2p and Co 2p spectra remain largely unchanged (see Figure S11b,c, Supporting Information) but display broadening, likely due to overlap with Ni LMM-2 Auger lines.<sup>[30]</sup> No significant changes are observed in the Li 1s and O 1s spectra (see Figure S10d,e, Supporting Information).

For pristine NCA, the Ni 2p<sub>3/2</sub> spectrum shows peak at 855.1 eV likely corresponds to  $\text{Ni}(\text{OH})_2$ ,<sup>[31]</sup> (see Figure 4f). After recycling, broadening of the Ni 2p<sub>3/2</sub> is observed, supported by the broadening in O 1s spectra (Figure S9k,l, Supporting Information). No significant binding energy shifts are observed in Co 2p (Figure S11d, Supporting Information) and Al 2p (Figure S11e, Supporting Information) spectra for recycled NCA. However, noticeable peak broadening suggests surface-level modifications. Furthermore, the Li signal in Li 1s (Figure S10f, Supporting Information) is significantly reduced after recycling, which may be attributed to the dissolution of Li ions.

Overall, the combination of XRD and XPS results demonstrates that the recycling process primarily affects the surface properties of electrode materials while largely preserving their bulk chemical states. Surface modifications, including the formation of hydroxides, halides, and changes in oxidation states, highlight the importance of understanding and mitigating surface degradation during recycling (see section 2.4).

Although XRD detected no structural differences in the electrode materials before and after recycling, XPS revealed notable surface alterations. To assess whether these surface changes affect the overall morphology, SEM analysis was conducted (Figure 5). The results indicate negligible changes in morphology between pristine and recycled electrode materials.

Additionally, it is worth noting that the recovery of LFP is highly sensitive to variations in processing steps, with significant differences observed depending on the synthesis method employed (solid-state synthesis vs. sol-gel process). Specifically, when LFP is synthesized via the sol-gel method, a carbon coating is applied, as confirmed by TEM analysis (Figure S13, Supporting Information). This carbon layer plays a pivotal role in modulating the recycling outcome, as indicated by diffraction analysis, where larger amounts of additional LiCl phase are observed alongside  $\text{Li}_3\text{InCl}_6$  for noncoated LFP. In addition, noncoated LFP undergoes partial decomposition during the dissolution-based separation process, as shown in the Supporting Information (see Figure S12, Supporting Information) based on two separate experimental batches. This results in the formation of additional phases, including  $\text{FePO}_4$ ,  $\text{Fe}_3\text{O}_4$ ,  $\text{FeO}$ , and other unidentified phases. Moreover, in addition to the desired  $\text{Li}_3\text{InCl}_6$  phase, a detectable amount (ranging from 3.63 to 7.66 wt%) of LiCl is observed. A comparative analysis of the diffraction patterns (Figure 1a vs. Figure S12, Supporting Information) suggests that the carbon coating may mitigate the interaction between  $\text{Li}_3\text{InCl}_6$  and the electrode material. In strong contrast to this, complete recrystallization of  $\text{Li}_3\text{InCl}_6$  is observed following the separation of  $\text{Li}_3\text{InCl}_6$  from C-LFP. However, XPS measurements (Figure 3d) still reveal the presence of indium species on the particle surfaces, indicating that some degree of interaction persists despite the carbon coating. These findings underscore the potential of surface modification, induced by specific coatings, to influence the interactions between electrode materials and solid electrolytes. The implementation of such surface modifications may represent a promising strategy to enhance the recycling efficiency of both the electrolyte and electrode materials.

Furthermore, it is essential to note that storing of the synthesized electrode materials in an Ar-filled glovebox is relevant for the quality of the recrystallized  $\text{Li}_3\text{InCl}_6$  (see section 2.4). When electrode materials were exposed to ambient air for a certain period prior to recycling, a higher amount of LiCl within the recrystallized  $\text{Li}_3\text{InCl}_6$  structure is detectable. For instance,  $\text{Li}_3\text{InCl}_6$  in combination with LTO, stored in ambient air after synthesis ( $\approx$ 1–2 weeks), shows a significantly larger LiCl phase fraction within the recycled sample compared to storage under Ar-atmosphere after synthesis. As illustrated in Figure S14, Supporting Information, the LiCl formation results in a higher phase fraction of LiCl (14.74 wt%), compared to the LTO sample stored in the Ar-filled glovebox (0.92 wt%). This increase is likely

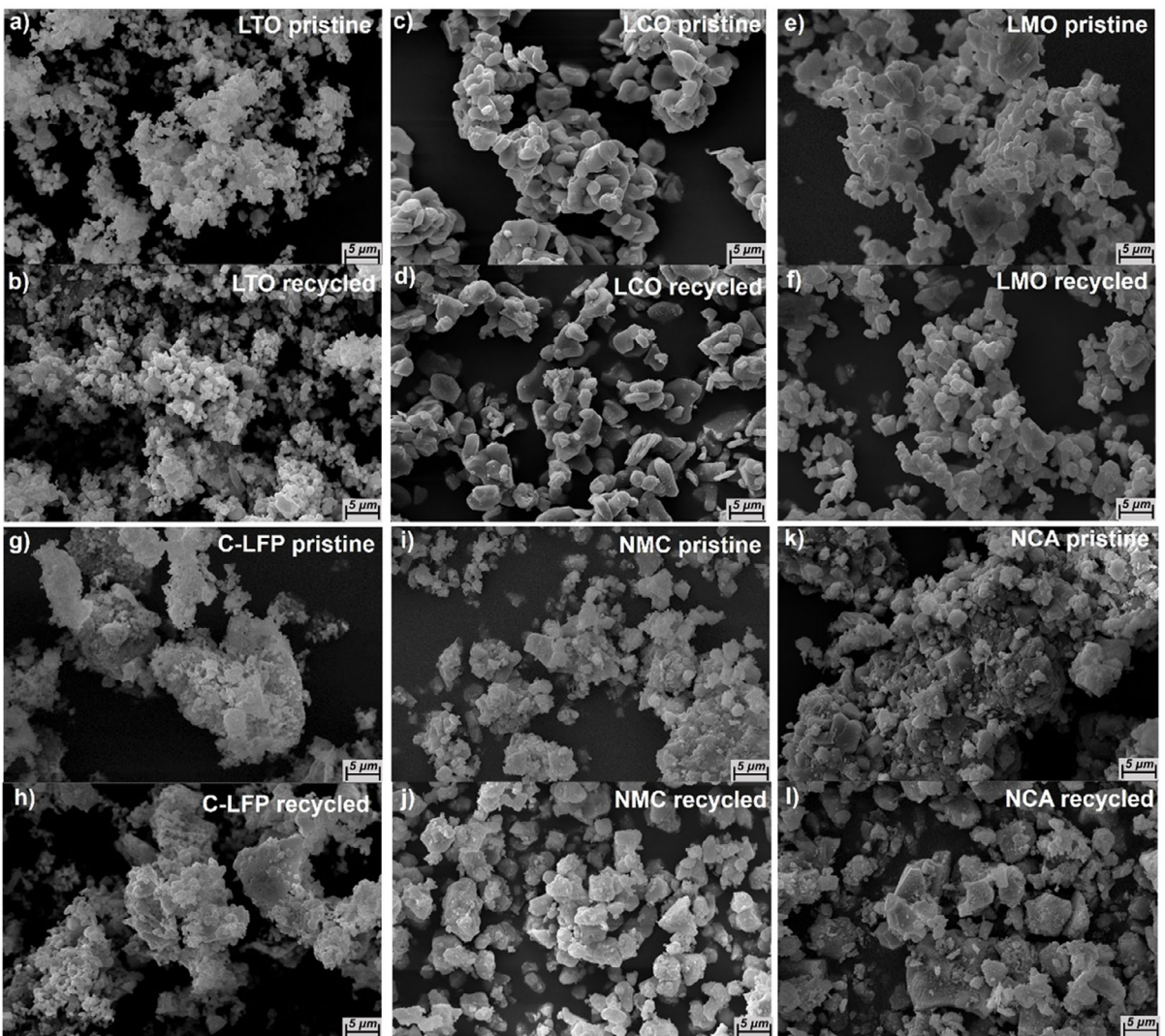


**Figure 5.** SEM images of pristine and recycled electrode materials: a) pristine LTO, b) recycled LTO, c) pristine LCO, d) recycled LCO, e) pristine LMO, f) recycled LMO, g) pristine C-LFP, h) recycled C-LFP, i) pristine NMC, j) recycled NMC, k) pristine NCA, and l) recycled NCA.

associated with  $\text{CO}_2$  absorption processes from the air, leading to the formation of  $\text{Li}_2\text{CO}_3$  and further promoting the Lewis acid–base mechanism, described in section 2.4.

#### 2.4. Deriving the Interaction Mechanism of Oxides in Aqueous $\text{Li}_3\text{InCl}_6$ Solutions

XPS characterization confirms the formation of an In-rich layer on the surface of the electrode materials, indicating interactions between oxide-based electrode materials and the solid electrolyte  $\text{Li}_3\text{InCl}_6$  dissolved in  $\text{H}_2\text{O}$ . To elucidate the underlying mechanism (see Figure 6), the reaction processes of oxide-based electrode materials in  $\text{H}_2\text{O}$  and the dissolution behavior of  $\text{Li}_3\text{InCl}_6$  in  $\text{H}_2\text{O}$  are examined.

Upon contact with  $\text{H}_2\text{O}$ , the surfaces of oxide-based materials develop a charge due to deprotonation of functional groups at the solid/liquid interface.<sup>[15,32,33]</sup> Active electrode materials (e.g., LTO, LCO, LMO, C-LFP, NMC, and NCA) undergo a lithium-proton exchange mechanism ( $\text{Li}^+/\text{H}^+$ ) at their surfaces, leading to the

formation of lithium hydroxide ( $\text{LiOH}$ ), when immersed in aqueous solution, creating a basic solution ( $\text{pH} > 7$ ).<sup>[15,17]</sup> pH measurements (see Table S8, Supporting Information) confirm basic behavior across all active materials, and Ni-rich electrode materials show higher pH levels compared to others, consistent with literature findings.<sup>[15,16]</sup>

The surface charge of electrode particles was determined via zeta-potential measurements (see Table S8, Supporting Information), which indicated a negatively charged particle surface. This negative charge is likely a result of cation dissolution (likely  $\text{Li}^+$  ion), followed by proton adsorption, leading to the formation of hydroxyl groups.

Upon dissolving  $\text{Li}_3\text{InCl}_6$  in water, the ions (e.g.,  $\text{Li}^+$ ,  $\text{In}^{3+}$ ,  $\text{Cl}^-$ ) become hydrated and build individual solvation shells.  $\text{In}^{3+}$  acts as a Lewis acid, forming an aqua complex in water  $[\text{In}(\text{H}_2\text{O})_6]^{3+}$ , which can undergo  $n$  deprotonation steps to form the hydrolyzed species  $[\text{In}(\text{H}_2\text{O})_{6-n}(\text{OH})_n]^{(3-n)+}$ , eventually leading to the formation of  $\text{In}(\text{OH})_3$ . The mechanisms can be described as follows.<sup>[34]</sup>

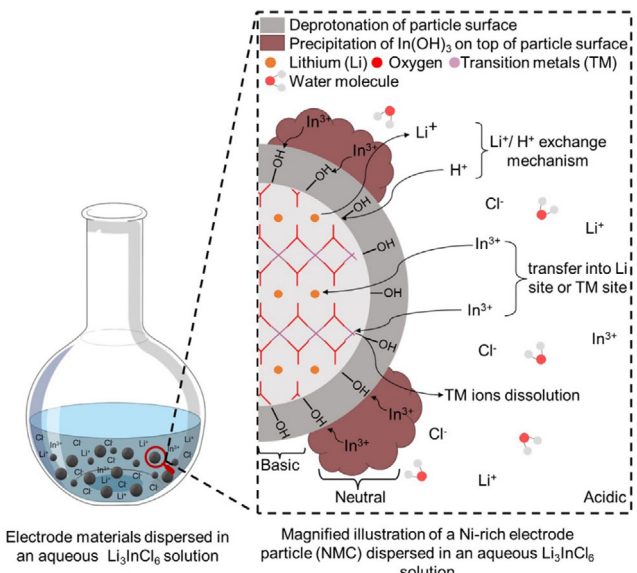
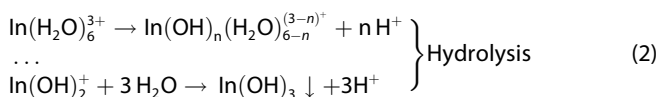
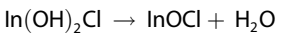


**Figure 6.** Schematic illustration depicting the underlying degradation mechanism.  $\text{Li}_3\text{InCl}_6$  is dissolved in  $\text{H}_2\text{O}$ , dissociating into ions, while the electrode materials are dispersed in  $\text{H}_2\text{O}$ .  $\text{Li}^+$ ,  $\text{In}^{3+}$ , and  $\text{Cl}^-$  ions surround the electrode particles. The recycling process follows a Lewis-acid and Lewis-base reaction mechanism, where hydroxyl groups on the oxide surface generate negatively charged particles acting as Lewis bases. These particles attract Lewis-acid  $\text{In}^{3+}$  ions, leading to the precipitation of  $\text{In}(\text{OH})_3$ .  $\text{Li}^+$  and TM ions dissolve, and  $\text{In}^{3+}$  may potentially replace these lattice positions.



Thus, interactions during the recycling process are consistent with a typical Lewis-acid and Lewis-base reaction mechanism. At the surface of the oxide, hydroxyl groups are formed, resulting in a negatively charged particle surface that behaves as a Lewis base. Surrounded by them, solvated ions (e.g.,  $\text{Li}^+$ ,  $\text{In}^{3+}$ ,  $\text{Cl}^-$ ) originating from  $\text{Li}_3\text{InCl}_6$  interact with these locally altered pH conditions. pH of a pure  $\text{Li}_3\text{InCl}_6$  solution is  $\approx 4$ , meaning that within an acidic solution, localized basic conditions emerge around the particles of the electrode material. The Lewis-acid  $\text{In}^{3+}$  is attracted to the negatively charged particle surface, and the proximity of the  $\text{In}^{3+}$  ion and the elevated pH at the particle surfaces promotes the precipitation of  $\text{In}(\text{OH})_3$  or other In-OH species on the particle surface.<sup>[35,36]</sup>

The extent of  $\text{In}(\text{OH})_3$  precipitation increases with the pH of the electrode material until the particle surface becomes neutral. In addition to the  $\text{In}(\text{OH})_3$  phase, other chemical species represented by phases such as  $\text{In}_2\text{O}_3$ ,  $\text{InOCl}$ , and  $\text{InCl}_3$  can form due to the specific chemical nature of the electrode material.  $\text{In}_2\text{O}_3$  and  $\text{InOCl}$  can be obtained through dehydration of  $\text{In}(\text{OH})_3$  and  $\text{In}(\text{OH})_2\text{Cl}$  (see Equation (3) and (4)), respectively.



Given that the recovered electrode material is not subjected to additional heat treatment after filtration, the formation of  $\text{In}_2\text{O}_3$  and  $\text{InOCl}$  species may also partly originate from the high vacuum conditions applied during XPS measurements. During the recycling process, in addition to the  $\text{Li}^+/\text{H}^+$  exchange mechanism, TMs from the electrode materials may dissolve into water, allowing  $\text{In}^{3+}$  ion to replace a TM in the lattice near the particle surface. Due to the higher solubility of the  $\text{Li}^+$  cation compared to  $\text{In}^{3+}$  cation, only indium precipitates under these conditions. This behavior can be attributed to the higher charge of indium, which results in the formation of less soluble compounds, while lithium remains in solution.<sup>[37]</sup> Further, lithium usually precipitates in the form of  $\text{LiOH}$  and  $\text{Li}_2\text{CO}_3$  at higher pH levels of 13–14 and, or high lithium concentrations, which could explain why Li is not precipitating along with In.<sup>[38]</sup>

According to this mechanism, the variation in the amount of  $\text{LiCl}$  in the recycled  $\text{Li}_3\text{InCl}_6$  is influenced by the basicity of the environment surrounding the electrode surface. This effect is particularly evident in Ni-rich electrode materials and in electrode materials with  $\text{Li}_2\text{CO}_3$  present on the particle surface, which promote enhanced indium precipitation. The significant loss of indium to the electrode surface leads to insufficient indium concentration in the solution, disrupting the  $\text{Li}-\text{In}-\text{Cl}$  stoichiometry. This imbalance prevents the complete recrystallization of  $\text{Li}_3\text{InCl}_6$ , thereby facilitating the formation of  $\text{LiCl}$  as an impurity.

## 2.5. Effect of Interactions on Electrochemical Properties

As demonstrated in section 2.3, significant interactions occur between the electrolyte and electrode materials during recycling. In this section, a systematic comparison of pristine and recycled electrolyte and electrode materials is conducted to evaluate the impact of these interactions on electrochemical properties. EIS was employed to analyze all electrolyte materials, while galvanostatic cycling, rate capability studies, and CV were performed on the electrode materials to assess variations in electrochemical performance.

### 2.5.1. Ionic Conductivity of Electrolyte Materials

**Figure 7a,b** displays the Nyquist plot and ionic conductivities at 25 °C of pristine, redissolved, and recycled  $\text{Li}_3\text{InCl}_6$  after separation from different electrode materials. In all cases the Nyquist plots exhibit a single semicircle at high frequencies, indicative of bulk ion conduction, while a capacitive response is observed at low frequencies across all samples, reflecting a blocking effect for the  $\text{Li}^+$  at the gold-sputtered electrodes. The impedance data were fitted using an equivalent circuit model consisting of one R-CPE ( $R$  = resistor, CPE = constant phase element) and a CPE element connected in series for bulk ion conduction and capacitive response, respectively.

The ionic conductivity of pristine  $\text{Li}_3\text{InCl}_6$ , as determined from the fitting, is  $9.68 \times 10^{-4} \text{ S cm}^{-1}$ , which is slightly lower than the

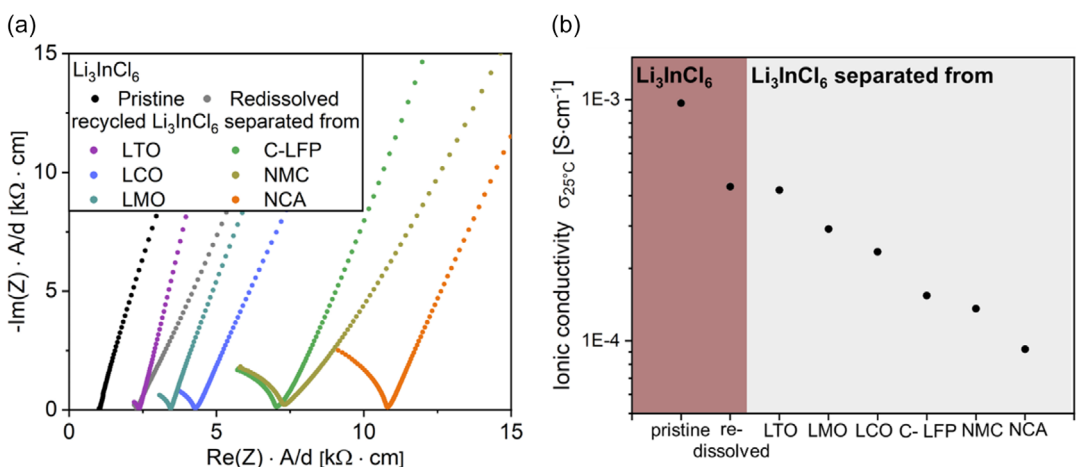


Figure 7. a) Nyquist plot and b) ionic conductivity at 25 °C of pristine, redissolved, and recycled  $\text{Li}_3\text{InCl}_6$  after separation from different electrode materials.

previously reported value of  $2.05 \times 10^{-3} \text{ S cm}^{-1}$ .<sup>[8]</sup> This difference in ionic conductivity can be attributed to factors such as variations in powder and pellet preparation,<sup>[39]</sup> morphology,<sup>[40]</sup> pressing conditions, and slight atmospheric differences within gloveboxes.<sup>[41]</sup> However, these variations do not result in a significant discrepancy. More notable may be potential relative changes in ionic conductivity that may arise due to the recycling process.

The higher ionic conductivity observed for pristine  $\text{Li}_3\text{InCl}_6$  compared to the redissolved sample ( $4.23 \times 10^{-4} \text{ S cm}^{-1}$ ) may be attributed to subtle structural changes, as indicated by refined lattice parameters (see Table S1, Supporting Information). These changes, potentially involving a low degree of Li-In disorder, could influence Li-ion transport by altering the distribution of mobile  $\text{Li}^+$  species and modifying the local ionic pathways. Despite the successful recrystallization confirmed by XRD, the reduction in ionic conductivity suggests that the redissolution still affects  $\text{Li}^+$  ion mobility.

More broadly, redissolution has a distinct impact on the ionic conductivity of  $\text{Li}_3\text{InCl}_6$  with further variations observed in recycled samples, where the extent of deviation in ionic conductivity from that of the redissolved sample depends on the specific electrode materials from which  $\text{Li}_3\text{InCl}_6$  was separated. Impedance spectroscopy data, supported by Rietveld analysis of XRD data (see Figure 1a), indicate that interactions between  $\text{Li}_3\text{InCl}_6$  and electrode materials during recycling are generally disadvantageous, leading to the formation of undesirable phases, such as  $\text{LiCl}$  and other unidentified phases. The impact of these impurities on the ionic conductivity is shown in Table 1. A correlation between the concentrations of  $\text{LiCl}$  and impurity elements, as determined by ICP-MS analysis, and the measured ionic conductivity values is observed.

For recycled  $\text{Li}_3\text{InCl}_6$  after separation from LTO, the ionic conductivity remains comparable to that of the redissolved sample, indicating minimal impact from this electrode material. In contrast, recycled  $\text{Li}_3\text{InCl}_6$ , after separation from LCO, LMO, and C-LFP, exhibits a reduction in ionic conductivity, likely due to the presence of impurity phases, as revealed from Rietveld analysis of XRD data, and the incorporation of TM elements from the electrodes, as evidenced by ICP-MS analysis. The most pronounced decline in ionic conductivity is observed for nickel-rich electrode

Table 1. Influence of structural (XRD) and compositional (ICP-MS) variations on the ionic conductivity of  $\text{Li}_3\text{InCl}_6$ . The table summarizes the impurity weight fraction, elemental impurities, and their correlation with the measured ionic conductivity values.

Material	XRD Analysis		Elemental Impurity [wt%]	$\sigma_{25^\circ\text{C}} [\text{S cm}^{-1}]$
	$\text{Li}_3\text{InCl}_6$ [wt%]	$\text{LiCl}$ [wt%]		
Pristine $\text{Li}_3\text{InCl}_6$	100	–	–	$9.68 \times 10^{-4}$
Redissolved $\text{Li}_3\text{InCl}_6$	100	–	–	$4.36 \times 10^{-4}$
Recycled $\text{Li}_3\text{InCl}_6$ separated from				
LTO	98.84	1.16	–	$4.22 \times 10^{-4}$
LCO	96.60	3.40	–	$2.34 \times 10^{-4}$
LMO	99.36	0.64	0.09 Mn	$2.91 \times 10^{-4}$
C-LFP	100	–	0.01–0.02 Fe	$1.54 \times 10^{-4}$
NMC	91.81	8.19	0.02 Ni	$1.36 \times 10^{-4}$
NCA	84.50	15.50	0.12 Ni, 0.04–0.05 Co, 0.20–0.21 Al	$9.23 \times 10^{-5}$

materials (e.g., NMC and NCA). This substantial decrease in ionic conductivity is likely attributable to a combination of impurity phases, compositional alterations, and changes in morphology or microstructure, particularly due to the agglomeration of particles within the recycled material.

While the individual contributions of elemental purity, crystallinity, and the presence of impurity phases (e.g., variation amount of  $\text{LiCl}$ , unknown phase) to the overall conductivity cannot be precisely deconvoluted, the findings of this study suggest that their interactions can, though not necessarily, result in complex variations in conductivity.

### 2.5.2. Voltammetric and Galvanostatic Assessment of Electrode Materials

Given the compositional changes from XPS analysis, the impact of these surface impurities on electrochemical performance was

further investigated. CV, galvanostatic cycling, and rate capability studies were conducted on both pristine and recycled electrode materials. For these experiments, half cells were constructed with electrode materials paired against lithium metal and a liquid electrolyte.

**Figure 8** presents the CV spectra for both pristine and recycled electrode materials, with the corresponding oxidation and reduction potentials summarized in Table S9, Supporting Information. **Figure 9** shows the rate capability study and the calculated Coulombic efficiency from the galvanostatic cycling of all pristine and electrode materials at varying C-rates of C/10, C/5, C/2, and C, with additional cycling data provided in Figure S15, Supporting Information.

The CV comparison for the LTO electrode (Figure 8a) reveals well-defined, reversible redox peaks, demonstrating enhanced stability and increased redox currents in the recycled sample compared to the pristine material, suggesting improved electrode kinetics after recycling. This observation is further supported by galvanostatic cycling data (Figure 9a,b, and Figure S15a,b, Supporting Information), which indicate higher initial capacities for the recycled LTO sample relative to the pristine counterpart. Moreover, the rate capability study confirms the improved performance of the recycled material, which is maintained even after extended cycling. A similar trend is observed for the C-LFP electrode, where CV analysis (Figure 8d) reveals well-defined, reversible redox peaks at higher currents and superior stability over ten cycles in the recycled sample compared to the pristine material. This behavior is further validated by the galvanostatic and rate capability studies (Figure 9g,h, and Figure S15g,h, Supporting Information), which indicate enhanced capacities for the recycled C-LFP electrode.

The observed improvements in both capacity and overall rate capability for recycled LTO and C-LFP electrodes compared to their pristine counterparts are likely attributed to the presence of  $\text{In}_2\text{O}_3$  on the electrode surface, as confirmed by XPS analysis (see Figure 3). This impurity phase appears to enhance electrochemical performance, consistent with previous studies,<sup>[42,43]</sup> in which  $\text{In}_2\text{O}_3$  was intentionally applied as a surface coating on cathode materials. These studies suggest that an  $\text{In}_2\text{O}_3$  surface layer may function as a buffering interface, improving electrode–electrolyte interphase stability and enhancing electrochemical performance. Additionally, the  $\text{In}_2\text{O}_3$  coating may contribute to increased electrochemical activity by providing additional active sites and facilitating more efficient  $\text{Li}^+$  diffusion.

In contrast, XPS analysis of the recycled LMO electrode reveals surface modifications (Figure 3c), including the presence of  $\text{In}_2\text{O}_3$  and  $\text{In(OH)}_3$ . While similar surface modifications improved the electrochemical performance of recycled LTO and C-LFP, the CV comparison between pristine and recycled LMO (Figure 8c) indicates that these benefits are less pronounced for LMO. Although the electrode retains structural stability after recycling, a decrease in redox current is observed, suggesting a reduction in capacity, as supported by galvanostatic and rate capability studies (Figure 9e,f and Figure S15e,f, Supporting Information). The reduced redox activity and capacity retention may be attributed to the findings of XRD and XPS analysis. XRD results reveal the formation of a small amount of a  $\text{Li}_2\text{MnO}_3$  phase alongside the primary  $\text{LiMn}_2\text{O}_4$  phase in the recycled sample. Additionally, ICP-MS analysis confirms Mn ion dissolution from the electrode material. XPS analysis further indicates changes in the chemical composition of LMO, evidenced by a shift to higher binding energies in the Mn 2p spectrum, suggesting an increased proportion

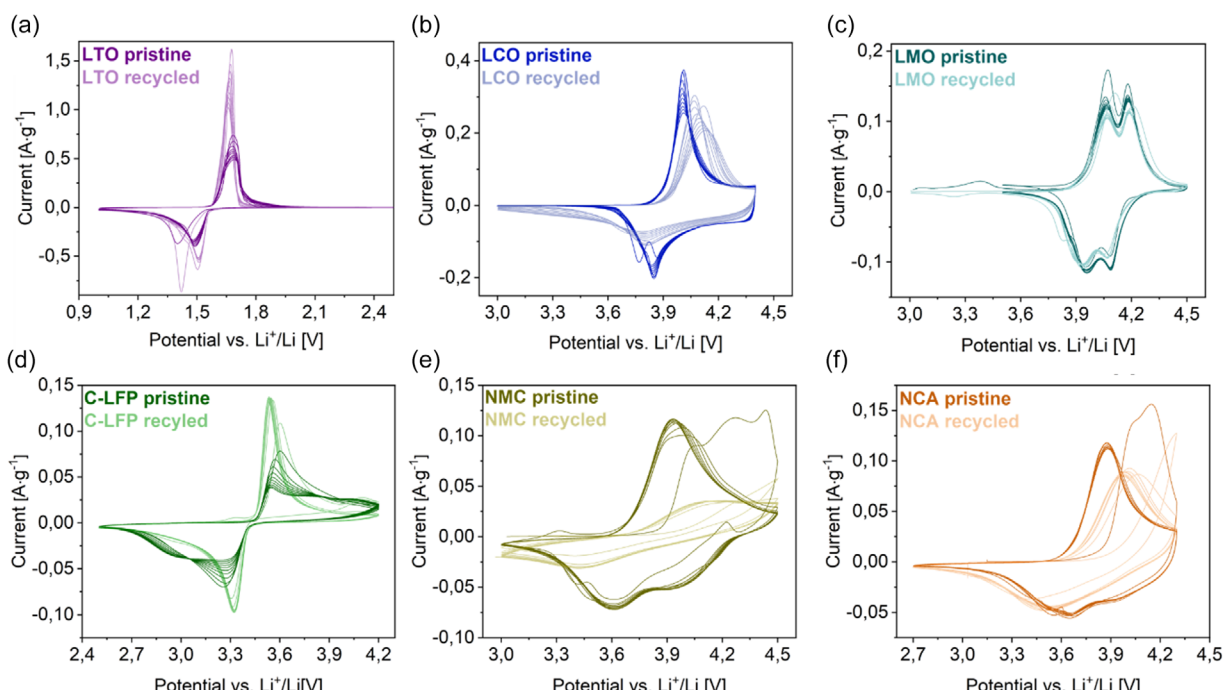


**Figure 8.** CV comparison spectra of pristine and recycled: a) LTO, b) LCO, c) LMO, d) C-LFP, e) NMC, and f) NCA.

of Mn in the +4 oxidation state, which may negatively impact electrochemical performance.

A more pronounced effect on electrochemical properties is observed when  $\text{InCl}_3$  is present on the particle surface (Figure 3c,e,f), as seen in layered structures (e.g., LCO, NMC, and NCA). The CV comparison of LCO (Figure 8c) reveals a significant reduction in redox currents, broadening of redox peaks, and progressive peak shifts with cycling, indicating deteriorating electrode kinetics and progressive surface degradation over continuous cycling. These effects suggest a higher-energy barrier for redox reactions, as reflected by higher redox potentials, indicating hindered charge transfer kinetics and reduced overall charge-transfer efficiency. Furthermore, the broadening of the redox peaks implies slower charge transfer dynamics and lower reversibility of the redox processes. The reduction in peak current correlates with a loss in electrochemical capacity, emphasizing material degradation after

recycling. These negative impacts are further shown by galvanostatic cycling and rate capability data (see Figure 9c,d and Figure S15c,d, Supporting Information), which demonstrate a continuous loss in both capacity and stability with each cycle.

These effects are even more pronounced in the CV comparison of NMC (Figure 8e) and NCA (Figure 8f), where a substantial decline in redox activity is observed. XPS analysis reveals a higher concentration of  $\text{InCl}_3$  on the surface, suggesting a more severe impact on electrochemical performance. However, it is important to note that  $\text{InCl}_3$  may dissolve from the surface during cycling, interacting with the electrolyte and altering electrochemical behavior. Consequently, the recycled NMC (see Figure 9i,j and Figure S15i,j, Supporting Information) and NCA (see Figure S9k,l and Figure S15k,l, Supporting Information) electrodes exhibit significantly reduced capacities and diminished redox reactivities, highlighting the negative influence of

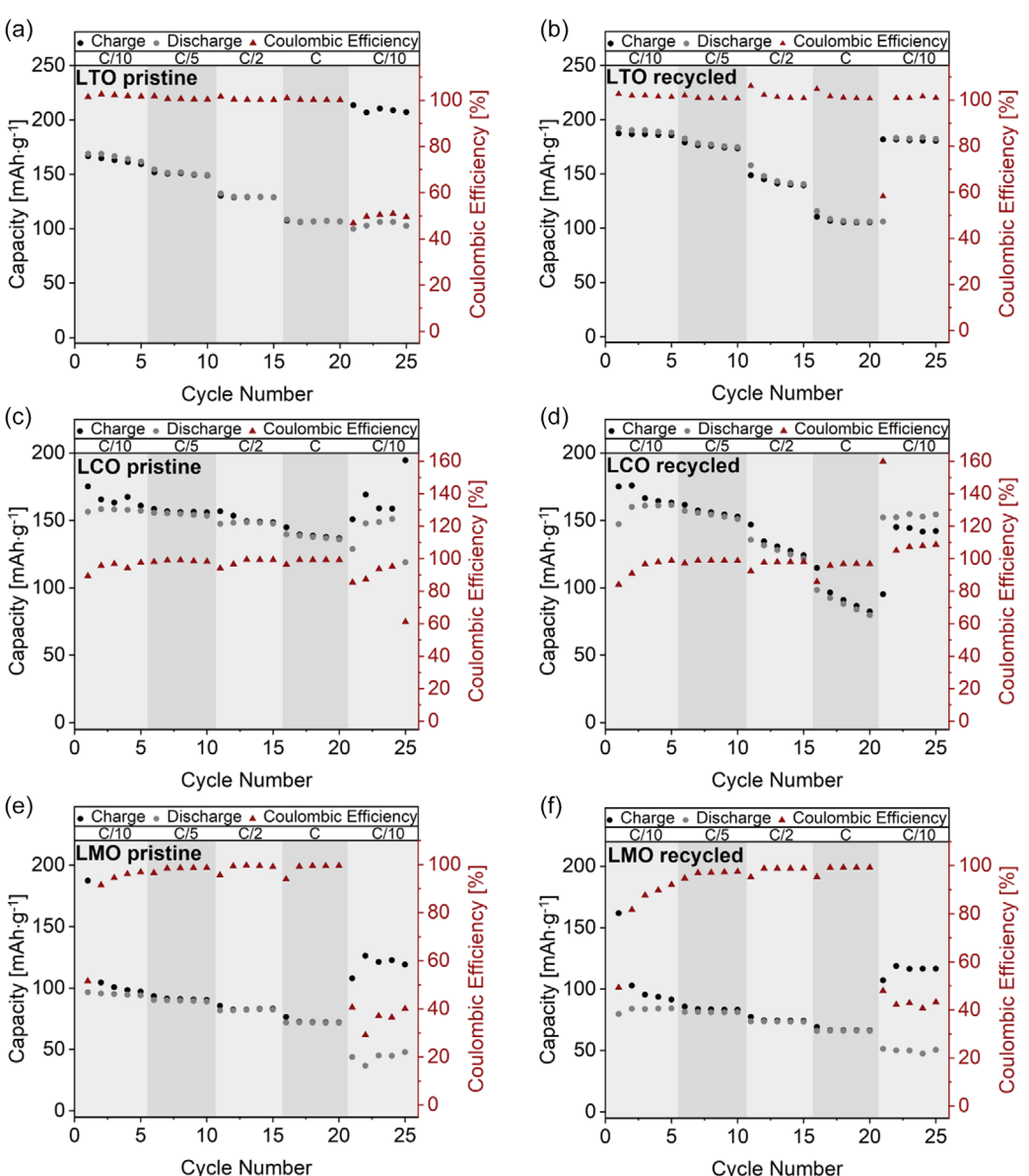


**Figure 9.** Rate capability study and Coulombic efficiency of pristine and recycled electrode materials: a) pristine LTO, b) recycled LTO, c) pristine LCO, d) recycled LCO, e) pristine LMO, f) recycled LMO, g) pristine C-LFP, h) recycled C-LFP, i) pristine NMC, j) recycled NMC, k) pristine NCA, and l) recycled NCA.

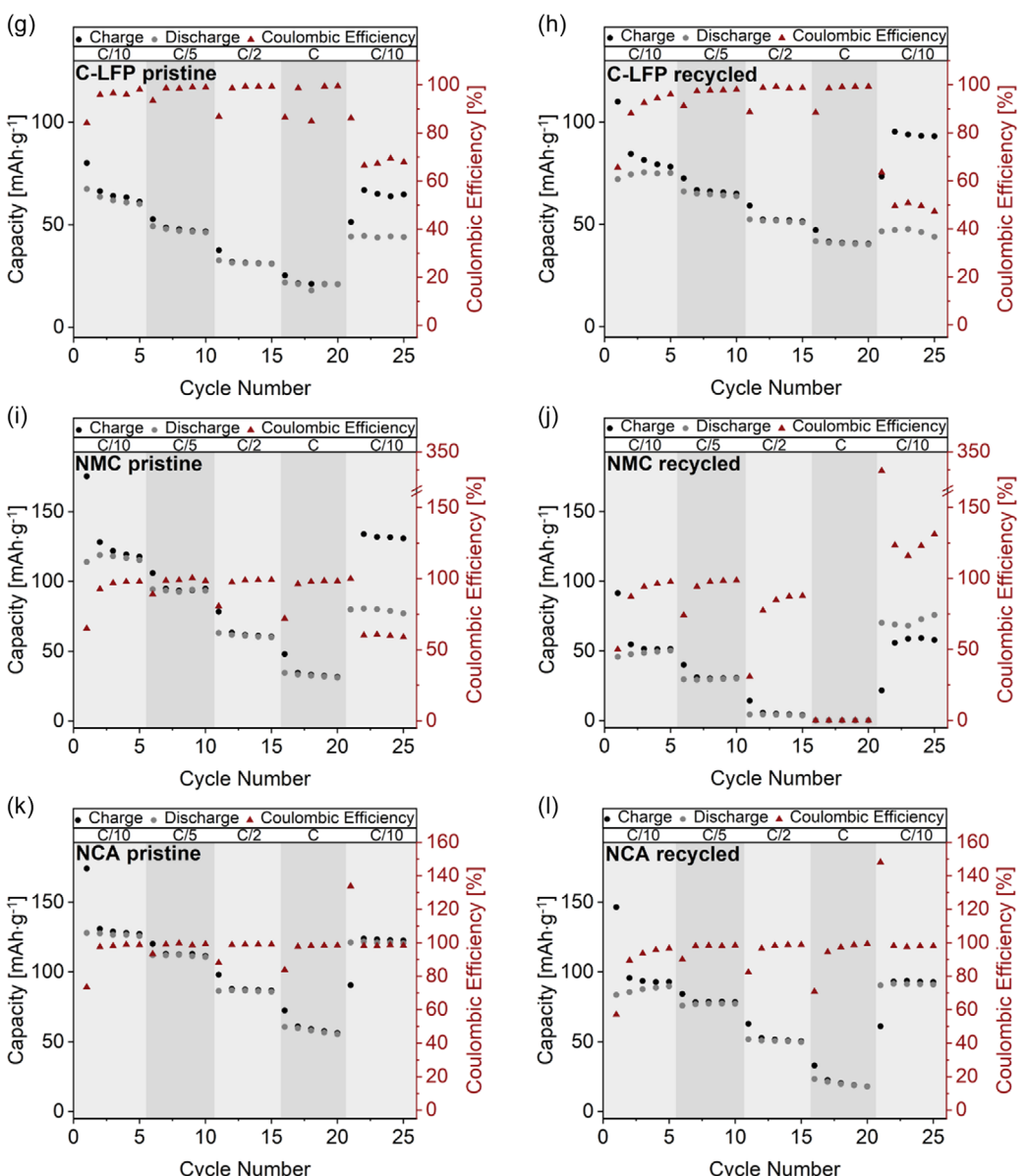


Figure 9. Continued.

InCl<sub>3</sub> on charge transfer kinetics and overall electrode stability. Halides, including InCl<sub>3</sub>, are highly soluble in organic liquid electrolytes, and their dissolution leads to interactions with electrolyte component during lithiation/delithiation, resulting in a complex electrochemical behavior poor electrochemical performance.<sup>[44]</sup>

These findings indicate that the presence of InCl<sub>3</sub> on the electrode surface adversely affects electrochemical performance, in contrast to the beneficial effects observed with In<sub>2</sub>O<sub>3</sub>. Future investigations would be valuable to assess how InCl<sub>3</sub>, present in recycled electrode materials, influences their cycling behavior in solid-state cells, particularly considering the observed poor electrochemical performance in half-cells with organic liquid electrolytes, where InCl<sub>3</sub> exhibits reactivity with the electrolyte. Such studies could provide deeper insights into the role of InCl<sub>3</sub> in solid-state battery systems and are planned for future investigations.

### 3. Conclusion

This study demonstrates that Li<sub>3</sub>InCl<sub>6</sub> can be effectively separated from different electrode materials (e.g., LTO, LCO, LMO, C-LFP, NMC, NCA). Notably, interactions between the solid electrolyte and electrode materials vary, with significantly greater reactivity observed for Ni-rich electrode materials. The recycling process follows a Lewis base–acid interaction mechanism, forming of In-containing phases (e.g., In–O, In–OH, and In–Cl species) via precipitation or ion exchange on electrode surfaces. Additionally, TM ions leach from the electrode framework into the Li<sub>3</sub>InCl<sub>6</sub> solution and are incorporated into the Li<sub>3</sub>InCl<sub>6</sub> structure after recrystallization. The presence of LiCl, unidentified secondary phases, and the extent of TMs incorporation into the Li<sub>3</sub>InCl<sub>6</sub> lattice significantly influence its ionic conductivity, generally resulting in an electrochemical performance degradation compared to the pristine electrolyte.

Despite achieving high-purity electrode recovery, the presence of indium-based impurities can either enhance or degrade the electrochemical performance of the electrodes, highlighting the need for post-processing to restore optimal electrochemical properties. Future efforts should focus on optimizing separation conditions and purification techniques to improve the reusability of  $\text{Li}_3\text{InCl}_6$  and enhance the cycling stability of recovered electrode materials.

These findings highlight the importance of integrating recyclability considerations into solid-state battery development processes to advance circular economic strategies for ASSBs. By improving recycling strategies and material recovery processes, this study contributes to advancing sustainable energy storage solutions for next-generation technologies.

## 4. Experimental Section

### Synthesis of $\text{Li}_3\text{InCl}_6$

$\text{Li}_3\text{InCl}_6$  was synthesized via a water-mediated synthesis route.<sup>[8]</sup> Stoichiometric amounts of anhydrous LiCl (Thermo Fisher Scientific, 98+) and anhydrous  $\text{InCl}_3$  (Thermo Scientific, 99.99%) were weighed inside an Ar-filled glovebox. Distilled  $\text{H}_2\text{O}$  in a ratio of 1 mL per 1 g was added and stirred for 15 min. The water was evaporated under continuous stirring inside an oil bath heated at 100 °C for 3 h, leading to a powder containing crystal water. The powder material was scraped out of the beaker and then ground using mortar and pestle. The powder was subsequently heated at 200 °C under vacuum for 8 h.

### Synthesis of Electrode Materials

$\text{Li}_4\text{Ti}_5\text{O}_{12}$  (LTO),  $\text{LiCoO}_2$  (LCO),  $\text{LiMn}_2\text{O}_4$  (LMO),  $\text{LiNi}_{0.8}\text{Mn}_{0.1}\text{Co}_{0.1}\text{O}_2$  (NMC), and  $\text{LiNi}_{0.8}\text{Co}_{0.15}\text{Al}_{0.05}\text{O}_2$  (NCA) were synthesized by solid-state reaction using  $\text{Li}_2\text{CO}_3$  (Alfa Aesar, 99%),  $\text{TiO}_2$  (Thermo Scientific, 99.6%),  $\text{Co}_3\text{O}_4$  (Thermo Fisher Scientific, 99.7%),  $\text{MnO}_2$  (Alfa Aesar, 99.9%),  $\text{NiO}$  (Thermo Fisher Scientific, 99%),  $\text{MnO}$  (Sigma Aldrich, 99%), and  $\text{Al}_2\text{O}_3$  (Alfa Aesar, 99%) as precursor materials. Stoichiometric amounts of the respective oxides were mixed at 300 rpm for 3 h via ball milling in a 25 mL  $\text{ZrO}_2$  milling jar with 10  $\text{ZrO}_2$  balls (diameter of 10 mm). For the milling process, isopropanol was used as a dispersant. The mixtures were calcined at 800–900 °C (heating and cooling rate of 3 °C min<sup>-1</sup>) in an  $\text{Al}_2\text{O}_3$  crucible between 10 and 12 h in ambient air. Additionally, an excess in  $\text{Li}_2\text{CO}_3$  of 10 wt% was added to the mixture to compensate for the loss of Li during thermal treatment. Carbon-coated LiFePO<sub>4</sub> (C-LFP) was synthesized via the sol-gel method,<sup>[45]</sup> using stoichiometric amounts of  $\text{NH}_4\text{H}_2\text{PO}_4$  (Alfa Aesar, 98%),  $\text{Fe}(\text{NO}_3)_3 \cdot 9 \text{ H}_2\text{O}$  (VWR Chemicals, 99%), and  $\text{LiNO}_3$  (Alfa Aesar, 99%), which were mixed in distilled water under continuous stirring. Citric acid (Sigma Aldrich, 99%) was added into the solution as a dispersant and carbon source, retaining a final carbon content of 4 wt%. Finally, ethylene glycol (Acros Organics, 99.5%) was added as a complexing agent to obtain a molar ratio of ethylene glycol to Fe ions of 1:1. The sol was homogenized and heated to 80 °C under constant stirring to evaporate the excess water and to form the gel. The dried precursor was decomposed at 400 °C (heating and cooling rate of 3 °C min<sup>-1</sup>) under Ar for 6 h, followed by intermediate hand grinding using a mortar and a pestle. After intermediate grinding, an additional heat treatment at 700 °C for 12 h with a heating rate of 5 °C min<sup>-1</sup> was conducted under an Ar atmosphere to obtain the C-LFP.

### Dissolution-Based Separation Processes

Equal amounts of pristine  $\text{Li}_3\text{InCl}_6$  and one of the above-given electrode materials (typically 0.75 g each) were mixed using mortar and pestle within an Ar-filled glovebox, forming a model black mass used for separation experiments. The mixture was transferred into a glass beaker and mixed with distilled  $\text{H}_2\text{O}$  in an ambient atmosphere. The resulting suspension was stirred for ≈15 min, followed by filtration of the suspended particles using filter paper (Carl Roth GmbH + Co. KG, Rotilabo-roundfilters, type 115A). The residue was rinsed thrice with distilled  $\text{H}_2\text{O}$ , dried in air, and stored in the glovebox. The filtrate was filtered a second time using a syringe filter (Sigma Aldrich, hydrophilic PTFE 0.2 μm Membrane), to remove residual electrode particles that passed through the filter paper. Afterward, the  $\text{H}_2\text{O}$  was evaporated at 100 °C under continuous stirring. The obtained powder was ground and further dried under vacuum at 200 °C for 8 h.

### X-ray Diffraction

The structural analysis of the pristine and the recycled materials was conducted using X-ray diffraction (XRD) with a SmartLab II instrument from Rigaku, Japan, employing Bragg-Brentano geometry and  $\text{CuK}_\alpha$  radiation. A HyPix 3000 detector operated in 1D mode was utilized. The diffraction patterns were obtained at room temperature with a 2° min<sup>-1</sup> scanning rate within the 2θ range of 10°–80°. Both pristine and recycled  $\text{Li}_3\text{InCl}_6$  samples were measured inside air-tight sample holders to prevent sample hydration. Pristine and recycled electrode materials were measured on zero-background single-crystal silicon substrates. The structural characteristics were determined using the Rietveld method as implemented in TOPAS V6 from Bruker AXS, Germany.

### Scanning Electron Microscopy and Energy-Dispersive X-ray

Scanning electron microscopy (SEM) and energy-dispersive X-ray (EDX) measurements were performed using a Zeiss EVO 15 device equipped with an integrated EDX system to study the morphology and composition of the pristine as-synthesized and recycled materials. Powder samples were fixed on an SEM sample holder using carbon tape and sputtered with gold. The sputtering was conducted inside an Ar-filled glovebox, to avoid oxidation and hydration of the air-sensitive solid electrolyte. Particle size distribution was analyzed using ImageJ software. A total of 100 individual particles were measured to obtain statistically representative size distribution data.

### Transmission Electron Microscopy

Transmission electron microscopy (TEM) investigations were carried out in a ThermoFisher Spectra 300 at 300 kV. The TEM was equipped with a high-brightness Schottky field emission gun. The scanning transmission electron microscopy images were recorded with a high-angle annular dark field detector using a dwell time of 10 μs. The camera length was set to 115 mm and the convergence angle to 22.5 mrad. The chemical composition was measured by EDX analysis. For this, TEM was equipped with a Thermo Fisher Super-X EDX detector.

### X-ray Photoelectron Spectroscopy

The investigation of particle surface of pristine and recycled electrode materials was examined using X-ray photoelectron spectroscopy (XPS). XPS spectra were acquired using a SPECS PHOIBOS 150 spectrometer implemented at the DAISY-FUN cluster tool. It was equipped with an Al  $K_\alpha$  X-ray source (monochromatic Focus 500 with XR50 M (SPECS),  $h\nu = 1486.74$  eV). Survey and detail spectra were measured in fixed analyzer transmission mode while choosing a pass energy of

20 eV (step size of 0.5 eV) for the survey and 10 eV (step size of 0.05 eV) for the core levels. The system was calibrated to 0.00 eV binding energy of the Fermi level of sputter-cleaned Au and Cu as well as emission lines of Au 4f<sub>7/2</sub> at 83.98 eV, Ag 3d<sub>5/2</sub> at 368.26 eV, and Cu 2p<sub>3/2</sub> at 932.67 eV binding energy with deviations  $\leq$  0.1 eV. The data analysis was performed with CasaXPS, version 2.3.18. The core-level spectra were fit with a Shirley background and peaks of a GL(30) line shape.

### Inductively Coupled Plasma Mass Spectrometry

Quantitative elemental analysis of the pristine, redissolved, and recycled Li<sub>3</sub>InCl<sub>6</sub> after separation from different electrode materials via inductively coupled plasma mass spectrometry (ICP-MS) was conducted with an Agilent ICP-MS system 8900 with triple quadrupole (ICP-QQQ) and SPS4 autosampler. The corresponding SSEs were weighed as a doublet for sample preparation into centrifuge tubes (Ultra-High Performance Centrifuge Tube, VWR International) in a glovebox under Ar-atmosphere. Then 10 mL ultrapure water (0.055  $\mu$ S cm<sup>-2</sup>, PURELAB Chorus 1 ultrapure water filtration unit, Elga LabWater) was added to the samples, and those were dissolved overnight on the shaking plate (Promax 1020 platform shaker, Heidolph Instruments) at ambient conditions. For the measurement, these solutions were diluted by factors of 50, 2000, and 20 000. A solution containing 10 mg L<sup>-1</sup> Sc (1 g L<sup>-1</sup> in 5% HNO<sub>3</sub>, Alfa), Y (1 g L<sup>-1</sup> in 2%–3% HNO<sub>3</sub>, Merck Certipur), and Ho (1 g L<sup>-1</sup> in 2%–3% HNO<sub>3</sub>, Merck Certipur) in ultrapure water was prepared as an internal standard solution for all ICP-MS measurements. HNO<sub>3</sub> (ROTIPURAN Supra 69%, Carl Roth) was used to acidify the measurement solutions, and argon 5.0 (Ar  $\geq$  99.999 mol%, ALPHAGAZ 1 Argon, Air Liquide) was used as plasma gas for ICP-MS measurements. The measurements were carried out with different cell gas modes. The analytes <sup>27</sup>Al, <sup>47</sup>Ti, <sup>55</sup>Mn, <sup>56</sup>Fe, <sup>59</sup>Co, <sup>60</sup>Ni, and <sup>115</sup>In were measured in He collision gas mode. <sup>7</sup>Li, <sup>27</sup>Al, and <sup>115</sup>In were additionally measured without any cell gas. H<sub>2</sub> reaction gas mode was used to measure <sup>35</sup>Cl via the mass pair (Q<sub>1</sub>, Q<sub>2</sub>) = (35, 37). To determine the P content, <sup>31</sup>P was measured via the mass pair (Q<sub>1</sub>, Q<sub>2</sub>) = (31, 47) using O<sub>2</sub> reaction gas mode. External calibrations were performed to quantify all elements using the following ICP-MS standard solutions: Li (1 g L<sup>-1</sup> in 0.5 M HNO<sub>3</sub>, Merck Certipur), Al (1 g L<sup>-1</sup> in 0.5 M HNO<sub>3</sub>, Bernd Kraft), P (1 g L<sup>-1</sup> in water, AccuStandard AccuTrace), Ti (1 g L<sup>-1</sup> in water tr. HF, VWR International), Mn (1 g L<sup>-1</sup> in 0.5 M HNO<sub>3</sub>, Fluka), Fe (1 g L<sup>-1</sup> in 0.5 M HNO<sub>3</sub>, Merck Certipur), Co (1 g L<sup>-1</sup> in 0.05 M HNO<sub>3</sub>, Fluka), Ni (1 g L<sup>-1</sup> in 0.05 M HNO<sub>3</sub>, Fluka), and In (1 g L<sup>-1</sup> in 0.05 M HNO<sub>3</sub>, Fluka). For the Cl calibration HCl (Suprapur 30%, Merck) was diluted accordingly.

### Electrochemical Impedance Spectroscopy

Electrochemical impedance spectroscopy (EIS) was employed to characterize the ionic conductivity of pristine, redissolved, and recycled Li<sub>3</sub>InCl<sub>6</sub> and electrode materials. Pellets composed of 100 mg powdered material were uniaxially pressed within a die of 7 mm diameter using a pressure of 2 ton for 10 min. The pellets were sputter coated with a thin layer of gold on both sides to ensure uniform electrical contact over the whole pellet surface. Impedance measurements were performed over a temperature range of 20 to 80 °C, with incremental steps of 5 °C. These measurements were conducted using a TSC battery cell from rhd instruments GmbH & Co, coupled with a NEISYS electrochemical impedance analyzer from Novocontrol Technologies, applying an AC signal of 10 mV over a frequency range from 1 MHz to 0.1 Hz. Data analysis was carried out using RelaxIS software from rhd instruments, Germany.

### Galvanostatic Cycling and Cyclic Voltammetry

Pristine and recycled electrode materials were tested in half-cell configuration against a lithium metal anode and liquid electrolyte. The electrodes were prepared by mixing the active materials with

conductive Super P carbon black and polyvinylidene difluoride (PVDF) binder in a weight ratio of 85:5:10. The binder solution comprised 10 wt% PVDF dissolved in N-methyl-2-pyrrolidone (NMP). Additional NMP was added to the slurry to adjust its viscosity. The resulting slurry was tape cast onto copper or aluminum foils using a doctor blade, yielding a wet film thickness of 180  $\mu$ m. The solvent was evaporated by placing the tape-cast films on a heating plate at 80 °C. After drying, 7.9 mm-diameter disks were punched from the foils and dried under vacuum at 80 °C for 12 h.

Two-electrode Swagelok-type cells were assembled inside an Ar-filled glovebox for electrochemical testing. These cells were built using prepared electrodes, lithium metal as the counter electrode, a glass fiber membrane-based separator (WhatmanGF/C), and a liquid electrolyte comprising 180  $\mu$ L of 1 M LiPF<sub>6</sub> in a 1:1 mixture of ethylene carbonate (EC) and diethyl carbonate (DEC). The assembled Swagelok cells were tested using a VMP potentiostat (BioLogic Science Instruments). Galvanostatic cycling with potential limitation was performed using different C rates of C/10, C/5, C/2, and C (five cycles for each C rate), with charge and discharge currents calculated based on the mass of the active material within the electrode tested. Moreover, cyclic voltammetry (CV) measurements were conducted for all electrode materials with a scan rate of 0.1 mV s<sup>-1</sup>.

### pH Measurements

250 mg of individual electrode materials were immersed in 25 mL H<sub>2</sub>O. The pH measurements were conducted at room temperature using a pH meter (Seven2Go pH/mV S2, pH accuracy  $\pm$ 0.01) after continuous stirring for 15 min.

### Zeta-Potential Measurements

A 100 mg sample of each pristine electrode material was immersed in 5 mL H<sub>2</sub>O and subjected to ultrasonic agitation for 15 min. Prior to the measurement, the dispersed electrode materials were mixed thoroughly using a vortex mixer, and 1 mL of the suspension was transferred into folded capillary zeta cells. Zeta-potential measurements were conducted at room temperature using a Zeta Sizer, Nano Series (Malvern Instruments).

### Acknowledgements

The authors acknowledge funding from the Alfred Kärcher-Förderstiftung. The elemental analysis group provided inductively coupled plasma mass spectrometry instrumentation for this work, with financial support from Saarland University and the German Science Foundation (project number INST 256/553-1). H.M.F. and J.P.H. acknowledge the German Federal Ministry of Education and Research (BMBF) for providing financial support within the cluster project PrometH2eus (Fkz: 03HY105H). Furthermore, the authors gratefully acknowledge the core facility SRF AMICA (Stuttgart Research Focus Advanced Materials Innovation and Characterization) at the University of Stuttgart for access to scanning electron microscopy and energy-dispersive X-ray equipment, as well as for their support and assistance with transmission electron microscopy use in this study. This research was supported by the German Research Foundation (DFG, AOBJ: 661806). Moreover, the authors would like to thank Nadine Sarkar for conducting zeta-potential measurements.

Open Access funding enabled and organized by Projekt DEAL.

## Conflict of Interest

The authors declare no conflict of interest.

## Data Availability Statement

The data that support the findings of this study are available from the corresponding author upon reasonable request.

**Keywords:** all-solid-state batteries · direct recycling · halide-based solid electrolytes · Li<sub>3</sub>InCl<sub>6</sub> · sustainability

- [1] L. Azhari, S. Bong, X. T. Ma, Y. Wang, *Matter* **2020**, *3*, 1845.
- [2] X. Wu, G. Ji, J. Wang, G. Zhou, Z. Liang, *Adv. Mater* **2023**, *35*, 2301540.
- [3] Y. Xiao, Y. Wang, S.-H. Bo, J. C. Kim, L. J. Miara, G. Ceder, *Nat. Rev. Mater.* **2020**, *5*, 105.
- [4] C. H. Wang, J. W. Liang, Y. Zhao, M. T. Zheng, X. N. Li, X. L. Sun, *Energy Environ. Sci.* **2021**, *14*, 2577.
- [5] M. Jacob, K. Wissel, O. Clemens, *Mater. Futures* **2024**, *3*, 012101.
- [6] Y. C. Bai, N. Muralidharan, Y. K. Sun, S. Passerini, M. S. Whittingham, I. Belharouak, *Mater. Today* **2020**, *41*, 304.
- [7] J. Neumann, M. Petranikova, M. Meeus, J. D. Gamarra, R. Younesi, M. Winter, S. Nowak, *Adv. Energy Mater.* **2022**, *12*, 2102917.
- [8] X. Li, J. Liang, N. Chen, J. Luo, K. R. Adair, C. Wang, M. N. Banis, T. K. Sham, L. Zhang, S. Zhao, S. Lu, H. Huang, R. Li, X. Sun, *Angew. Chem. Int. Ed. Engl.* **2019**, *58*, 16427.
- [9] J. Piatek, S. Afyon, T. M. Budnyak, S. Budnyk, M. H. Sipponen, A. Slabon, *Adv. Energy Mater.* **2021**, *11*, 2003456.
- [10] E. Fan, L. Li, Z. Wang, J. Lin, Y. Huang, Y. Yao, R. Chen, F. Wu, *Chem. Rev.* **2020**, *120*, 7020.
- [11] Y. Kim, S. Choi, *Acta Mater.* **2024**, *276*, 120135.
- [12] A. Banik, B. Samanta, B. Helm, M. A. Kraft, Y. Rudel, C. Li, M. R. Hansen, B. V. Lotsch, S. Bette, W. G. Zeier, *Inorg. Chem.* **2024**, *63*, 8698.
- [13] B. Warren, *Phys. Rev.* **1941**, *59*, 693.
- [14] T. Welberry, B. Butler, *J. Appl. Crystallogr.* **1994**, *27*, 205.
- [15] W. B. Hawley, A. Parejiya, Y. C. Bai, H. M. Meyer, D. L. Wood, J. L. Li, *J. Power Sources* **2020**, *466*, 228315.
- [16] M. Wood, Y. Sheng, T. J. Keever, J. Li, D. L. Wood, *Electrochemical Society Meeting Abstracts*, Vol. 231, The Electrochemical Society, Inc., Oak Ridge National Laboratory, USA **2017**, pp. 376–376.
- [17] M. Yang, L. Chen, H. Li, F. Wu, *Energy Mater. Adv.* **2022**, *2022*, 9842651.
- [18] M. Bichon, D. Sotta, N. Dupré, E. De Vito, A. Boulineau, W. Porcher, B. Lestriez, *ACS Appl. Mater. Interfaces* **2019**, *11*, 18331.
- [19] C. Zhan, T. Wu, J. Lu, K. D. Amine, *Energy Environ. Sci.* **2018**, *11*, 243.
- [20] C. Mahadevan, R. K. Meena, *Mater. Sci. Res. India* **2019**, *16*, 198.
- [21] M. Hirayama, H. Tomita, K. Kubota, H. Ido, R. Kanno, *Mater. Res. Bull.* **2012**, *47*, 79.
- [22] B. V. Crist, *Handbook of Monochromatic XPS Spectra: The Elements and Native Oxides*, XPS International, Inc., XPS International LLC, USA **1999**.
- [23] J. F. Moulder, W. F. Stickle, P. E. Sobol, K. D. Bomben, *Handbook of X-Ray Photoelectron Spectroscopy*, Perkin- Elmer Corporation, Physical Electronics Division, USA **1992**.
- [24] S. Hashimoto, A. Tanaka, *Surf. Interface Anal.* **2002**, *34*, 262.
- [25] R. Fantin, A. Van Roekeghem, A. Benayad, *Surf. Interface Anal.* **2023**, *55*, 489.
- [26] C. Schenck, J. Dillard, J. Murray, *J. Colloid Interface Sci.* **1983**, *95*, 398.
- [27] X. Hou, X. Liu, H. Wang, X. Zhang, J. Zhou, M. Wang, *Energy Storage Mater.* **2023**, *57*, 577.
- [28] Z. Yang, J. Gong, C. Tang, W. Zhu, Z. Cheng, J. Jiang, A. Ma, Q. Ding, *J. Mater. Sci.: Mater. Electron.* **2017**, *28*, 17533.
- [29] M. Hofmann, M. Kapuschinski, U. Guntow, G. A. Giffin, *J. Electrochem. Soc.* **2020**, *167*, 140535.
- [30] O. Bondarchuk, A. P. LaGrow, A. Kvasha, T. Thieu, E. Ayerbe, I. Urdampilleta, *Appl. Surf. Sci.* **2021**, *535*, 147699.
- [31] J. Gallenberger, H. M. Fernández, A. Alkemper, M. Li, C. Tian, B. Kaiser, J. P. Hofmann, *Catal. Sci. Technol.* **2023**, *13*, 4693.
- [32] K. W. Goh, M. R. Johan, Y. H. Wong, *Appl. Phys. A* **2016**, *122*, 907.
- [33] B. C. Bunker, W. H. Casey, *The Aqueous Chemistry of Oxides*, Oxford University Press **2016**.
- [34] L. Wang, D. Snihirova, M. Deng, C. Wang, D. Höche, S. V. Lamaka, M. L. Zheludkevich, *Electrochim. Acta* **2021**, *373*, 137916.
- [35] S. A. Wood, I. M. Samson, *Ore Geol. Rev.* **2006**, *28*, 57.
- [36] E. Chassaing, N. Naghavi, S. Galanti, G. Renou, M. Soro, M. Bouttemy, A. Etcheberry, D. Lincot, *ECS Trans.* **2013**, *50*, 93.
- [37] C. E. Housecroft, A. G. Sharpe, *Inorganic Chemistry*, Pearson Education, Edinburgh Gate Harlow Essex CM202JE, England **2018**.
- [38] H. Bae, Y. Kim, *Mater. Adv.* **2021**, *2*, 3234.
- [39] C. Schneider, C. P. Schmidt, A. Neumann, M. Clausnitzer, M. Sadowski, S. Harm, C. Meier, T. Danner, K. Albe, A. Latz, *Adv. Energy Mater.* **2023**, *13*, 2203873.
- [40] W. Du, J. Roa, J. Hong, Y. Liu, Z. Pei, C. Ma, *J. Manuf. Sci. Eng.* **2021**, *143*, 091002.
- [41] S. Ohno, T. Bernges, J. Buchheim, M. Duchardt, A.-K. Hatz, M. A. Kraft, H. Kwak, A. L. Santhosha, Z. Liu, N. Minafra, *ACS Energy Lett.* **2020**, *5*, 910.
- [42] M. Moustafa, F. Elmasry, *J. Sol-Gel Sci. Technol.* **2022**, *104*, 189.
- [43] S. Zhou, Z. Zhang, H. Wang, B. He, Y. Gong, J. Jin, X. Zhang, R. Wang, *Ionics* **2023**, *29*, 1323.
- [44] J. Liang, X. Li, J. T. Kim, X. Hao, H. Duan, R. Li, X. Sun, *Angew. Chem.* **2023**, *135*, e202217081.
- [45] S. Liu, H. Yin, H. Wang, H. Wang, *J. Nanosci. Nanotechnol.* **2014**, *14*, 7060.

Manuscript received: March 14, 2025

Version of record online: